Simultaneous NuSTAR/Chandra Observations of The Bursting Pulsar GRO J1744-28 During Its Third Reactivation

Younes, G.; Kouveliotou, C.; Grefenstette, B. W.; Tomsick, J. A.; Tennant, A.; Finger, M. H.; Fürst, F.; Pottschmidt, K.; Bhalerao, V.; Boggs, S. E.

Total number of authors:
12

Published in:
Astrophysical Journal

Link to article, DOI:
10.1088/0004-637X/804/1/43

Publication date:
2015

Document Version
Publisher's PDF, also known as Version of record

The Astrophysical Journal, 804:43 (16pp), 2015 May 1 doi:10.1088/0004-637X/804/1/43

SIMULTANEOUS *NuSTAR/CHANDRA* OBSERVATIONS OF THE BURSTING PULSAR GRO J1744-28 DURING ITS THIRD REACTIVATION

G. Younes[1,2], C. Kouveliotou[3,2], B. W. Grefenstette[4], J. A. Tomsick[5], A. Tennant[3,2], M. H. Finger[1,2], F. Fürst[4], K. Pottschmidt[6,7], V. Bhalerao[8], S. E. Boggs[5], L. Boirin[9], D. Chakrabarty[10], F. E. Christensen[11], W. W. Craig[5,12], N. Degenaar[13], A. C. Fabian[14], P. Gandhi[15], E. Göğüş[16], C. J. Hailey[17], F. A. Harrison[4], J. A. Kennea[18], J. M. Miller[11], D. Stern[19], and W. W. Zhang[20]

[1] Universities Space Research Association, 6767 Old Madison Pike, Suite 450, Huntsville, AL 35806, USA
[2] NSSTC, 320 Sparkman Drive, Huntsville, AL 35805, USA
[3] Astrophysics Office, ZP 12, NASA-Marshall Space Flight Center, Huntsville, AL 35812, USA
[4] Cahill Center for Astrophysics, 1216 East California Boulevard, California Institute of Technology, Pasadena, CA 91125, USA
[5] Space Sciences Laboratory, 7 Gauss Way, University of California, Berkeley, CA 94720-7450, USA
[6] Center for Space Science and Technology, University of Maryland Baltimore County, Baltimore, MD 21250, USA
[7] CRESST and NASA Goddard Space Flight Center, Astrophysics Science Division, Code 661, Greenbelt, MD 20771, USA
[8] Inter-University Center for Astronomy and Astrophysics, Post Bag 4, Ganeshkhind, Pune 411007, India
[9] Observatoire Astronomique de Strasbourg, 11 Rue de l'Université, F-67000 Strasbourg, France
[10] Kavli Institute for Astrophysics and Space Research, Massachusetts Institute of Technology, Cambridge, MA 02139, USA
[11] DTU Space, National Space Institute, Technical University of Denmark, Elektrovej 327, DK-2800 Lyngby, Denmark
[12] Lawrence Livermore National Laboratory, Livermore, CA 94550, USA
[13] Department of Astronomy, University of Michigan, 1085 South University Avenue, Ann Arbor, MI 48109, USA
[14] Institute of Astronomy, Madingley Road, Cambridge CB3 0HA, UK
[15] Department of Physics, Durham University, South Road, Durham DH1 3LE, UK
[16] Sabancı University, Orhanlı-Tuzla, İstanbul 34956, Turkey
[17] Columbia Astrophysics Laboratory, Columbia University, New York, NY 10027, USA
[18] Department of Astronomy & Astrophysics, The Pennsylvania State University, 525 Davey Lab, University Park, PA 16802, USA
[19] Jet Propulsion Laboratory, California Institute of Technology, Pasadena, CA 91109, USA
[20] NASA Goddard Space Flight Center, Greenbelt, MD 20771, USA
Received 2014 December 2; accepted 2015 February 18; published 2015 April 29

ABSTRACT

We report on a 10 ks simultaneous *Chandra*/High Energy Transmission Grating (HETG)–*Nuclear Spectroscopic Telescope Array (NuSTAR)* observation of the Bursting Pulsar, GRO J1744-28, during its third detected outburst since discovery and after nearly 18 yr of quiescence. The source is detected up to 60 keV with an Eddington persistent flux level. Seven bursts, followed by dips, are seen with *Chandra*, three of which are also detected with *NuSTAR*. Timing analysis reveals a slight increase in the persistent emission pulsed fraction with energy (from 10% to 15%) up to 10 keV, above which it remains constant. The 0.5–70 keV spectra of the persistent and dip emission are the same within errors and well described by a blackbody (BB), a power-law (PL) with an exponential rolloff, a 10 keV feature, and a 6.7 keV emission feature, all modified by neutral absorption. Assuming that the BB emission originates in an accretion disk, we estimate its inner (magnetospheric) radius to be about 4×10^7 cm, which translates to a surface dipole field $B \approx 9 \times 10^{10}$ G. The *Chandra*/HETG spectrum resolves the 6.7 keV feature into (quasi-)neutral and highly ionized Fe XXV and Fe XXVI emission lines. XSTAR modeling shows these lines to also emanate from a truncated accretion disk. The burst spectra, with a peak flux more than an order of magnitude higher than Eddington, are well fit with a PL with an exponential rolloff and a 10 keV feature, with similar fit values compared to the persistent and dip spectra. The burst spectra lack a thermal component and any Fe features. Anisotropic (beamed) burst emission would explain both the lack of the BB and any Fe components.

Key words: pulsars: general – stars: individual (GRO J1744-28) – X-rays: binaries – X-rays: bursts

1. INTRODUCTION

GRO J1744-28 is a high-energy transient in a low-mass X-ray binary (LMXB) system, and only the second source, besides the Rapid Burster (Lewin et al. 1993), observed to emit multiple type II X-ray bursts, i.e., due to spasmodic accretion rather than thermonuclear burning. The source was discovered in 1996 with the Burst and Transient Source Experiment on board the *Compton Gamma Ray Observatory*, when it emitted a series of hard X-ray bursts during a period lasting ~150 days (Kouveliotou et al. 1996). Soon after its discovery, Finger et al. (1996a) reported that the timing properties of the persistent X-ray emission pointed toward a magnetized neutron star pulsating at 2.14 Hz, accreting material from a low-mass companion in a nearly circular orbit with an orbital period of 11.8 days. At that time GRO J1744-28 was the first source to show bursts and pulsations, hence the source was nicknamed "the Bursting Pulsar" (hereafter BP). The BP emerged from quiescence again almost exactly 1 yr after its first outburst, in 1996 December (Woods et al. 1999). This second outburst was very similar to the first including both burst and persistent X-ray emission characteristics (Woods et al. 1999).

The BP and its two outbursts were studied extensively during the first few years after its discovery. The X-ray bursts from the source were classified as type II bursts, based on their spectra, energetics (Kouveliotou et al. 1996), and their resemblance to the bursts observed from the Rapid Burster (Lewin et al. 1996). Type II bursts are most likely the result of some sort of instability (whose origin is still unknown) in the

accretion disk resulting in the onset of mass inflow onto the neutron star, which is responsible for the bursting activity. The BP average burst duration was 10 s, and each burst was followed by a dip in flux below that of the pre-burst persistent emission. The flux recovered exponentially back to the pre-burst persistent emission level on timescales of a few hundred seconds (Giles et al. 1996; Strickman et al. 1996; Borkus et al. 1997; Aleksandrovich et al. 1998; Aptekar et al. 1998a, 1998b; Woods et al. 1999; Mejía et al. 2002). Pulsations at the spin frequency of the source were also detected during bursts, albeit with an average time lag of about 50 ms compared to the pre-burst pulses (Stark et al. 1996; Strickman et al. 1996; Koshut et al. 1998; Woods et al. 2000). The pre-burst pulse profile (PP) was subsequently recovered on timescales of a few hundred seconds (Stark et al. 1996). Miller (1996) attributed these lags to the accretion column geometry at the pole.

There is no direct estimate as yet of the magnetic field of the BP. Finger et al. (1996a; see also Daumerie et al. 1996) placed an upper limit on the dipole magnetic field of $B \lesssim 6 \times 10^{11}$ G based on the spin-up rate of the source and the persistent pulsed luminosity. Rappaport & Joss (1997) deduced from binary evolution calculations that the dipole magnetic field of GRO J1744-28 lies in the range of $(1.8–7.0) \times 10^{11}$ G, with a most probable value of 2.7×10^{11} G. Finally, Cui (1997) derived a surface magnetic field of $B \approx 2.4 \times 10^{11}$ G, assuming that the propeller effect is the reason for the non-detection of X-ray pulsations when the source persistent flux dropped below a certain level. It is, therefore, likely that the surface magnetic field of the BP lies between classical X-ray accreting pulsars ($\sim 10^{12}$ G) and LMXBs ($\sim 10^{9}$ G). This intermediate strength surface field could be an important parameter defining the unusual properties of this source; hence, the determination of its exact value is of crucial importance.

Nishiuchi et al. (1999) studied the 0.5–10 keV spectrum of GRO J1744-28 during outbursts using ASCA. They found a spectrum well described by an absorbed power-law (PL) and line-like emission between 6 and 7 keV, most likely from Fe reprocessed in the accretion disk. The heavy absorption toward the source ($N_{\rm H} \approx 10^{23}$ cm^{-2}) places the BP at the Galactic center, likely at 8 kpc.

The quiescent X-ray counterpart of the BP was discovered with *Chandra* (Wijnands & Wang 2002) and was confirmed 1 month later with *XMM-Newton* (Daigne et al. 2002). The spectrum in quiescence is soft and could be fit with either a PL model with $\Gamma = 2–5$ or a blackbody (BB) with $kT = 0.4–1$ keV, implying a quiescent 0.5–10 keV X-ray luminosity of 3×10^{33} erg s^{-1} at 8 kpc. Using the *Chandra* position, Gosling et al. (2007; see also Augusteijn et al. 1997; Cole et al. 1997) found two potential infrared counterparts within the BP error circle, with the most likely candidate being a giant star of type G4 III.

On 2014 January 18, the *Monitor of All-sky X-ray Image* Gas Slit Camera detected enhanced hard X-ray emission from the Galactic center region (Negoro et al. 2014b). Following the detection, they examined archival data from the *Swift* Burst Alert Telescope (BAT) and found that the X-ray emission from the BP had increased compared to its quiescent level. Soon after, the source triggered BAT on 2014 January 18 (Negoro et al. 2014b). Finger et al. (2014) detected pulsations from the direction of GRO J1744-28 at the 2.14 Hz spin period of the source during January 19.0–21.0 using the *Fermi* Gamma-ray Burst Monitor. Finally, the *Swift* X-ray Telescope (XRT) observed the BP on 2014 February 2 (Kennea et al. 2014), detecting a bright source at the *Chandra* location, confirming that the source entered a new outburst after about 18 yr of quiescence (see also Chakrabarty et al. 2014; D'Ai et al. 2014; Linares et al. 2014; Negoro et al. 2014a; Pandey-Pommier et al. 2014; Pintore et al. 2014; Sanna et al. 2014). Masetti et al. (2014) discovered infrared brightening of the G4 III candidate counterpart contemporary with the X-ray outburst, confirming its identification as the BP companion.

Here we report our results of the analysis of a 10 ks simultaneous *Chandra* and *Nuclear Spectroscopic Telescope Array* (*NuSTAR*) observation of the BP taken on 2014 March 3. Section 2 describes the observations and data reduction techniques. Our results are presented in Section 3 and discussed in Section 4.

2. OBSERVATIONS AND DATA REDUCTION

2.1. Chandra

We observed the BP with *Chandra* using the High Energy Transmission Grating (HETG) in continuous clocking mode (CC-mode) with all six CCDs of the ACIS-S array. The HETG comprises two sets of gratings, the medium-energy grating (MEG), operating in the energy range of 0.4–7 keV, and the high-energy grating (HEG), with energy coverage in the range of 0.8–10 keV and a spectral resolution (FWHM) $\Delta E = 0.4 - 77$ eV. Each grating spectrum is dispersed along the ACIS-S CCDs into positive and negative spectral orders. In addition, each grating observation results in an on-axis undispersed image with the CCD spectral resolution. We used the CC-mode to obtain the highest possible temporal resolution of 2.85 ms, at the expense of obtaining a one-dimensional image of the source.

The observation took place on 2014 March 3, 08:59:06 UTC, with 10 ks of good time intervals. A comparison between the zeroth order and the dispersed HEG $\pm$ first-order light curve reveals that the bursts are completely missing from the zeroth-order light curve due to heavy pileup. The source persistent emission also suffered a 10% pileup effect in the zeroth order. On the other hand, the dispersed grating spectra have a much lower total count rate compared to that of the zeroth-order spectra. This results in spectra free of pileup except during the peak of the bursts when pileup still occurred at the 10% level.

To use the grating arms in our timing analysis, the photons assigned times needed to be corrected for their diffraction angle, which is directly proportional to the grating time offset with respect to the zeroth order. This time offset, δt, relative to the zeroth-order location is

$$\delta t = -\frac{\sin\,(tg\_r_{\rm i}) \times X_{\rm R} \times \sin\,\alpha_{\rm i}}{\Delta_{\rm p}} t_{\rm p}[s], \qquad (1)$$

where $tg\_r_{\rm i}$ is the diffraction angle of each photon i, $X_{\rm R}$ is the Rowland spacing, $\alpha_{\rm i}$ is the grating clocking angle, $\Delta_{\rm p}$ is the pixel size, and $t_{\rm p}$ is the read time per row (2.85 ms).

The use of CC-mode with any *Chandra* grating observation introduces some complications to the data reduction and analysis.[21] For instance, due to the fact that there is no spatial information (the clocking rows are all collapsed into one

[21] http://cxc.harvard.edu/cal/Acis/Cal_prods/ccmode/ccmode_final_doc02.pdf

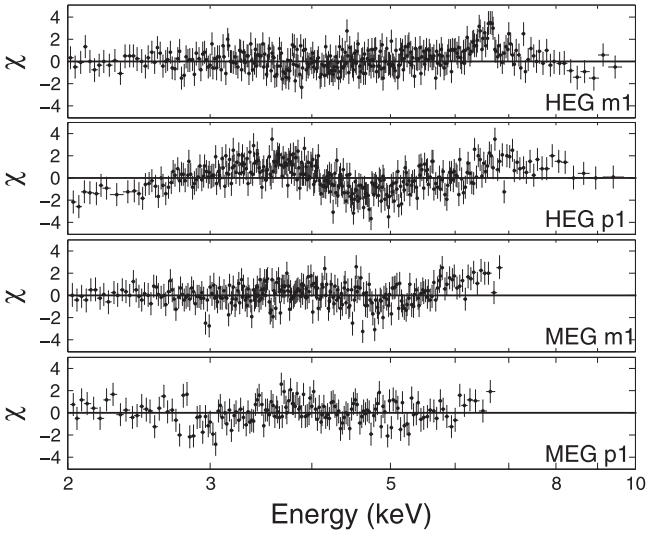

Figure 1. Residuals of an absorbed PL fit to the non-burst emission interval for the + and − arms of both the HEG and MEG first order spectra. The wiggle seen in the HEG p1 spectrum between 2 and 6 keV is not detected in any of the other three spectra. We conclude that this shape is artificial and refrain from using the HEG p1 in the non-burst spectral analyses.

pixel), the soft X-ray background, usually low in TE mode, is enhanced by 3 orders of magnitude.

A more pressing issue, which can alter grating dispersed spectra in CC-mode, is the dust scattering halo, usually present around bright absorbed sources. The BP resides in the Galactic center region; hence, it is heavily absorbed, with a hydrogen column density $N_{\rm H} \approx 10^{23}$ cm^{-2}. The brightness of the source produces a diffuse scattering halo, the emission from which disperses and blends with the source dispersed spectrum. The significance of this effect depends on the incident source spectrum, with hard sources affected less than soft ones. Luckily, the BP has a hard X-ray spectrum (Section 3.3), which reduces the impact of this background on the source spectrum.

Since no spatial information exists when using CC-mode, we extract the MEG and HEG backgrounds using the order sorting plots, which display the energies of the dispersed events versus the ratios of these energies over the event positions on the grating arm[1]. On-axis point-source photons should distribute tightly and symmetrically around the extraction order, while diffuse photons have a larger scatter. Finally, the extracted background is normalized to the excluded source region. These backgrounds are used for both timing and spectral analyses.

In addition to the background complications when dealing with CC-mode observations, there are calibration uncertainties[1] between the different orders, e.g., complicated charge transfer inefficiency corrections on the events. To check for potential differences, all *Chandra* analyses were initially performed on the separate HEG and MEG arms. Temporal analysis returned consistent results between all the different arms. Spectral analyses, on the other hand, showed that the HEG p1 (hereafter, p1 refers to the positive and m1 to the negative first-order grating arms) spectrum is markedly different from the rest, i.e., MEG p1, MEG m1, and HEG m1. Figure 1 shows a PL fit to the different spectral arms, where a wiggle between 2 and 6 keV is present only in the HEG p1 spectrum. We conclude that this feature is not real, and most likely due to either miscalibration, an improper modeling of the background, or both. Hence, the HEG p1 arm is excluded from the spectral analyses, except for bursts, where the above feature is not present (likely due to the small integration times during bursts and/or the fact that the emission during burst intervals includes minimal background).

All narrow features in the *Chandra* spectra are seen above 6 keV. Due to the lower spectral resolution and collecting area of the MEGs at energies $\gtrsim$5 keV, we also exclude these spectra in the analysis. For our timing analyses, we use the HEG first-order gratings (positive and negative arms combined, i.e., HEG 1).

2.2. NuSTAR

The *NuSTAR* is a NASA Small Explorer satellite launched on 2012 June 13 (Harrison et al. 2013). It is the first orbiting focusing hard X-ray telescope, observing the sky in an energy range from 3 to 79 keV with two co-aligned X-ray optics that focus X-rays onto two independent detector planes (FPMA and FPMB), each composed of four CdZnTe detectors. The field of view of *NuSTAR* is roughly $12' \times 12'$ with a point-spread function with an FWHM of $18''$ and a half-power diameter of $58''$.

NuSTAR obtained simultaneous observations of the BP during the *Chandra* observation. The broader *NuSTAR* BP data set is reserved for future work; here we concentrate on the data obtained simultaneously with *Chandra*. We reduced the *NuSTAR* data using NuSTARDAS v 1.3.1 and the *NuSTAR* CALDB 20131210, with the standard pipeline filtering. We extracted the source photons from a circular region with a radius of $60''$; these regions were centroided separately for FPMA and FPMB to account for the small misalignments in the absolute aspect reconstruction for the two telescopes.

NuSTAR produces event files (e.g., each row in the event file represents a single time-tagged photon), which we can then filter based on the source region described above to produce "source" event files.

We produced response files (ARFs and RMFs) for the *NuSTAR* spectral analysis using the custom time intervals defined in Section 3.1. These response files capture the response of the instrument over the specified time ranges.

3. RESULTS

3.1. Temporal Properties

We show in Figure 2 the 2–10 keV *Chandra* HEG first-order light curve (top panel) of the entire 10 ks observation, with 10 s time bins. Seven bursts are detected from the source during this observation. Following each burst, a dip in the count rate is observed, which recovers exponentially back to the persistent level. The FPMA light curve of the simultaneous *NuSTAR* observation is shown in the second panel in Figure 2, in the energy range of 3–10 keV and also at 10 s resolution. Only three bursts are detected simultaneously by both *Chandra* and *NuSTAR*. Figure 3 is a zoom-in on these three bursts plotted with a 0.5 s resolution.

We use a Bayesian Blocks algorithm (Scargle et al. 2013) to identify the beginning and end times of the seven bursts detected with *Chandra*, and to search for weaker bursts in the *Chandra* light curve binned with 0.5 s resolution. We chose this temporal resolution as a trade-off between speed and accuracy, considering that the source has a comparable pulse period. Bayesian Blocks have been frequently used for the

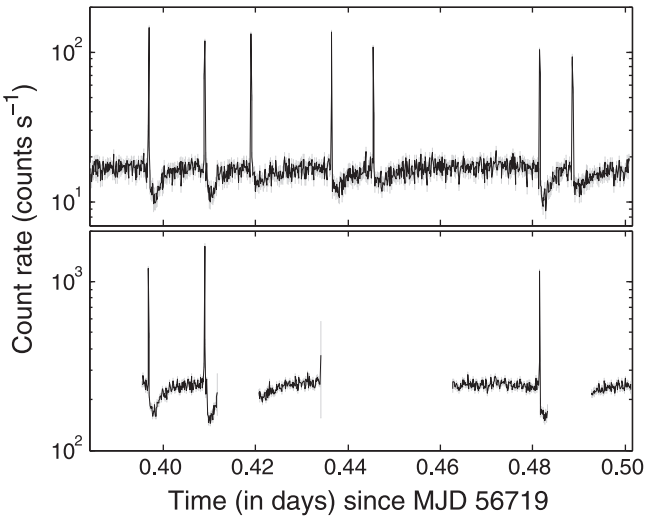

Figure 2. *Chandra* (top panel) and *NuSTAR* (bottom panel) light curves in the 2–10 and 3–10 keV energy ranges, respectively. Both light curves are binned with 10 s time resolution. A total of three bursts are detected simultaneously by *Chandra* and *NuSTAR*.

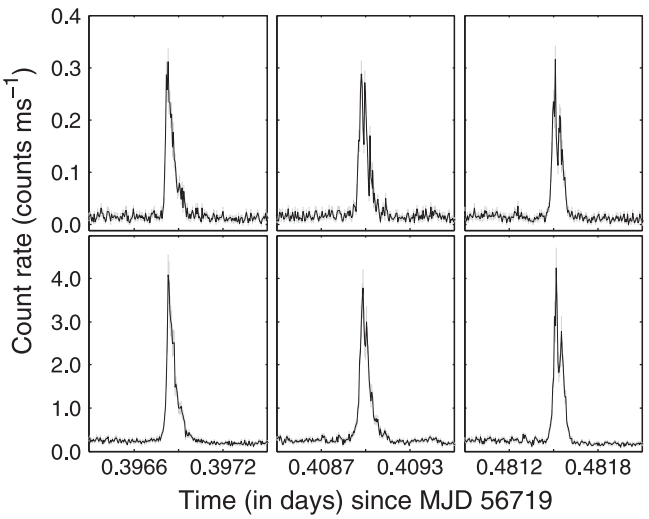

Figure 3. Light curves of the three bursts that are covered simultaneously by *Chandra* (top panel) and *NuSTAR* (bottom panel) in the 2–10 and 3–10 keV energy ranges, respectively, plotted with 0.5 s time resolution.

temporal analysis of gamma-ray bursts, magnetars, and even flares from Sgr A* (e.g., Norris et al. 2011; Nowak et al. 2012; Lin et al. 2013; Barrière et al. 2014). We find that only the seven bursts clearly visible in Figure 2 show significant deviations ($\gtrsim 5\sigma$) from the persistent level of the source. We do not find any weaker (mini-) bursts similar to the ones seen during the first two outbursts, e.g., (Nishiuchi et al. 1999).

The start and end times of the seven *Chandra* bursts are recorded from the Bayesian Blocks analysis (Figure 4). Table 1 shows these start times in MJD, and durations in seconds. The uncertainty on these durations is dominated by the temporal resolution we used, and it is $\leqslant 1$ s ($\leqslant 0.5$ s error at the beginning and end of each burst). All durations, except the last, are narrowly distributed with a mean and 1σ standard deviation of 12 ± 2 s. The last burst consists of two pulses with a total duration of 25 s (Figure 4). The rise and decay times of all bursts have a mean and 1σ standard deviation of 4.0 ± 1.0 s and 8.0 ± 2.0 s, respectively (excluding the decay time of the last burst).

We identify the dip durations using the following method on the 2–10 keV *Chandra* light curve binned at 10 s. We search for the time bin with the minimum count rate immediately after the end of a burst and up to the start of the following burst (the end of the observation after the last burst). We then fit the light curve of each of these time intervals with an exponential function of the form

$$C(t) = \left(C_{\rm p} - C_{\rm min}\right)\left(1 - \exp\left\{-(t - t_{\rm min})/\tau\right\}\right) + C_{\rm min}, \quad (2)$$

where $C_{\rm min}$ is the minimum count rate at time $t_{\rm min}$, $C_{\rm p}$ is the persistent count rate level, and τ is the characteristic timescale representing 63.2% recovery of the count rate to $C_{\rm p}$. We first performed fits keeping both $C_{\rm p}$ and τ as free parameters. We find that $C_{\rm p}$ is similar in all cases with good enough coverage after the recovery; hence, we keep $C_{\rm p}$ constant at the mean count rate value calculated from time intervals far away from bursts and dips (black solid line in Figure 5). Figure 5 shows in red our exponential fits to the dips, and Table 2 lists the dip temporal properties. We find that τ ranges between 112 and 246 s, with a mean and 1σ standard deviation of 191 ± 43 s, whereas the average time from the end of a burst to the minimum count rate of the dip, $T_{\rm S\_dip}$, is 105 ± 27 s. We note that no bursts are seen during the dipping intervals, i.e., all bursts are emitted after the dip recovered to at least the 95% level of the persistent emission. The gray areas in Figure 5 represent the persistent emission time intervals excluding bursts and dip intervals.

Finally, we searched for any strong spectral variations in the *Chandra* observation, especially during bursts, by looking at the evolution of the source flux hardness ratio, H/S, where H includes the energy ranges 4–6 and 8–10 keV (to avoid contamination from the Fe line complex; see Section 3.3), and S includes the 2–4 keV range. The bottom panel of Figure 5 shows the H/S derived from light curves with a 0.5 s resolution during bursts and with 10 s bins elsewhere. We do not find any spectral variations during bursts in the *Chandra* observation compared to the non-burst emission, at the above temporal resolution.

3.2. PP Analysis

For each of the intervals defined in the previous section, we first apply a barycenter correction for the *Chandra* and *NuSTAR* time-tagged events (see also Section 2.1 for a description of the *Chandra* grating time correction). We then correct these times for the binary motion of the system, using the orbital parameters provided by the GBM pulsar team.[22] We estimate the spin frequency of the pulsar from the persistent data by locating the peak Rayleigh power, nR^2, in a frequency range expected to contain the spin frequency. The Rayleigh power is given by

$$nR^2 = \frac{1}{n}\left|\sum_{i=0}^{n-1}\exp\{2\pi\nu t_i\}\right|^2 \quad (3)$$

[22] http://gamma-ray.nsstc.nasa.gov/gbm/science/pulsars.html

Table 1
BP Burst Temporal and Spectral Properties

Burst #	Start Time (MJD)	Duration (s)	Rise (s)	Decay (s)	PL Norm.[a] (photons keV^{-1} cm^{-2} s^{1})	Flux[a,d] (10^{-8} erg cm^{-2} s^{-1})	Fluence[a,d] (10^{-7} erg cm^{-2})	Luminosity[a,b,d] (10^{38} erg s^{-1})	$\text{Flux}^{c}_{0.5\text{–}70\ \text{keV}}$ (10^{-8} erg cm^{-2} s^{-1})
1	56719.396802	13.5	2.8	10.8	8 (5–11)	8.6 (7.7–9.7)	11.6 (10.4–13.1)	6.6 (5.9–7.4)	10.5 (10.2–10.9)
2	56719.408920	15.5	4.8	10.8	7 (5–10)	7.4 (6.7–8.4)	11.5 (10.4–13.0)	5.7 (5.1–6.4)	9.3 (8.9–9.6)
3	56719.418949	12.5	5.0	7.5	8 (6–12)	9.2 (8.3–10.4)	11.5 (10.4–13.0)	7.1 (6.4–8.0)	…
4	56719.436373	9.0	3.5	5.5	10 (7–14)	10.7 (9.7–12.1)	9.7 (8.7–10.9)	8.2 (7.4–9.3)	…
5	56719.445465	11.0	3.5	7.5	7 (5–10)	7.3 (6.5–8.3)	8.3 (7.2–9.1)	5.6 (5.0–6.4)	…
6	56719.481460	12.5	5.3	7.3	7 (5–11)	8.2 (7.4–9.2)	10.2 (9.2–11.5)	6.3 (5.6–7.1)	9.4 (9.0–9.7)
7	56719.488544	25.0	2.3	22.3	5 (3–7)	5.3 (4.8–5.9)	13.1 (11.9–14.8)	4.0 (3.7–4.5)	…

[a] Absorbed PL with $N_{\rm H} = 9.0 \times 10^{22}$ cm^{-2}, and $\Gamma = 1.2$.
[b] Assuming a distance of 8 kpc.
[c] Combined *Chandra* and *NuSTAR* data fit with an absorbed *cutoffPL* with $N_{\rm H} = (10.0 \pm 1.0) \times 10^{22}$ cm^{-2}, $\Gamma = 0.5 \pm 0.1$, and $E_{\rm fold} = 8.8 \pm 0.7$ keV.
[d] Derived in the energy range 0.5–10 keV.

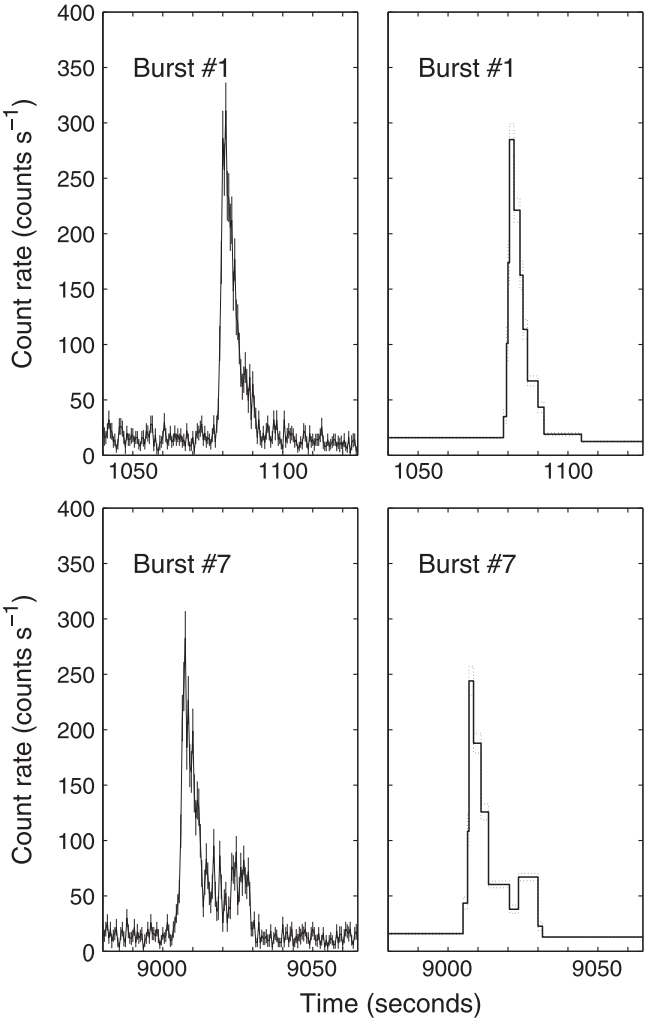

Figure 4. Two examples of *Chandra* 2–10 keV light curves of BP bursts with 0.5 s resolution (left panels), along with their Bayesian Blocks representation (right panels). Times are from the start of the *Chandra* observation.

(Brazier 1994), where n is the number of events, ν a trial frequency, and t_i a barycenter and binary corrected event time.

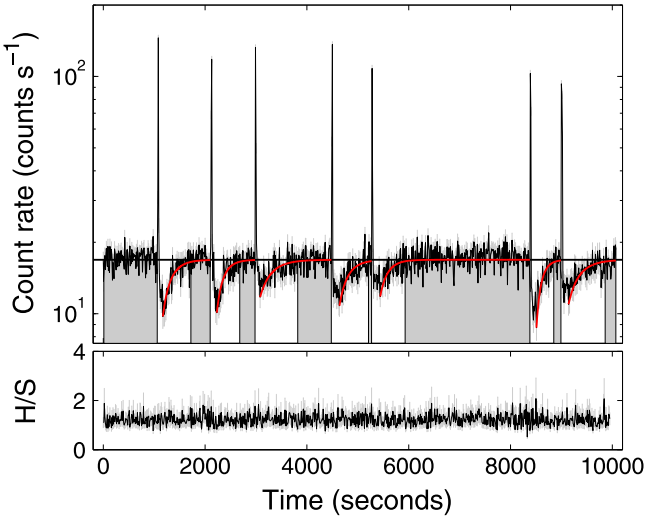

Figure 5. Top: *Chandra* 2–10 keV light curve with 10 s resolution. The black solid line is the mean rate of a pre-defined persistent emission interval far away from bursts and dips. The gray areas are the persistent emission intervals used in our spectral analysis. The red solid curves are exponential fits to the dip intervals. Bottom: Hardness ratio, H/S, evolution during the entire *Chandra* observation (H is computed in the 4–6 and 8–10 keV range, and S in the 2–4 keV range).

The peak power of 891 occurs at frequency 2.1411203(16) Hz. The 1σ error is determined by the change in frequency required for the Rayleigh power to drop by 0.5. Finally, we epoch-fold the data at the spin frequency derived above to compute a PP. For the persistent and dip intervals, we extract *Chandra* and *NuSTAR* PP in different energy bands, chosen to have comparable number of events (Figure 6).

We fit the different PPs with a sine plus cosine function of the form (Bildsten et al. 1997),

$$C(\phi) = C_{\rm mean} + \sum_{k=1}^{m}\left[A_k \sin(2\pi k\phi) + B_k \cos(2\pi k\phi)\right], \quad (4)$$

where $C(\phi)$ is the count rate at phase bin ϕ, $C_{\rm mean}$ is the average count rate throughout the PP, and A_k, B_k are the coefficients of the different harmonics k of the sine and cosine

Table 2
BP Dip Temporal and Spectral Properties

Dips #	$t_{\rm min}^{\rm a}$ (MJD)	$\tau^{\rm b}$ (s)	$T_{\rm S\_dip}^{\rm c}$ (s)	$F_{\rm avr,\ t\_min}^{\rm d}$ (10^{-9} erg cm^{-2} s^{-1})	$F_{\rm t\_min}^{\rm e}$ (10^{-9} erg cm^{-2} s^{-1})	Flux$_{\rm total}$ (10^{-8} erg cm^{-2} s^{-1})	Fluence$^{\rm f}$ (10^{-6} erg cm^{-2})	Flux$^{\rm g}_{0.5-70\ \rm keV}$ (10^{-8} erg cm^{-2} s^{-1})
1	56719.397861	182 ± 14	78	7.9 (6.9–9.2)	6.8 ± 0.3	1.00 (0.98–1.03)	1.3 (1.5–1.1)	2.2 (2.1–2.4)
2	56719.410129	147 ± 15	89	8.0 (7.0–9.3)	7.1 ± 0.2	1.03 (1.00–1.05)	1.0 (0.9–1.2)	…
3	56719.419967	246 ± 27	75	9.7 (8.6–11.3)	8.2 ± 0.3	1.09 (1.07–1.11)	1.1 (0.9–1.3)	…
4	56719.438023	189 ± 23	133	8.6 (7.6–10.0)	7.3 ± 0.3	1.02 (1.00–1.04)	1.4 (1.2–1.6)	…
5	56719.447282	162 ± 25	145	9.1 (8.1–10.6)	8.0 ± 0.3	1.06 (1.04–1.08)	1.0 (0.8–1.2)	…
6	56719.482814	112 ± 12	104	7.8 (6.9–9.1)	6.1 ± 0.3	0.95 (0.94–0.98)	1.2 (1.3–1.1)	…
7	56719.490106	239 ± 22	109	9.0 (7.9–10.4)	7.4 ± 0.3	1.03 (1.01–1.05)	1.5 (1.3–1.7)	…

[a] Dip times at minimum count rate after burst.
[b] Dip characteristic time-scale for recovery.
[c] Duration of interval from end of burst to $t_{\rm min}$.
[d] Calculated in an 80 s interval centered on $t_{\rm min}$.
[e] Calculated at $t_{\rm min}$ over 10 s by converting count rates to fluxes with PIMMS. Errors reflect the count rate errors only.
[f] Fluence deficiency in the dip.
[g] Combined *Chandra* and *NuSTAR* data.

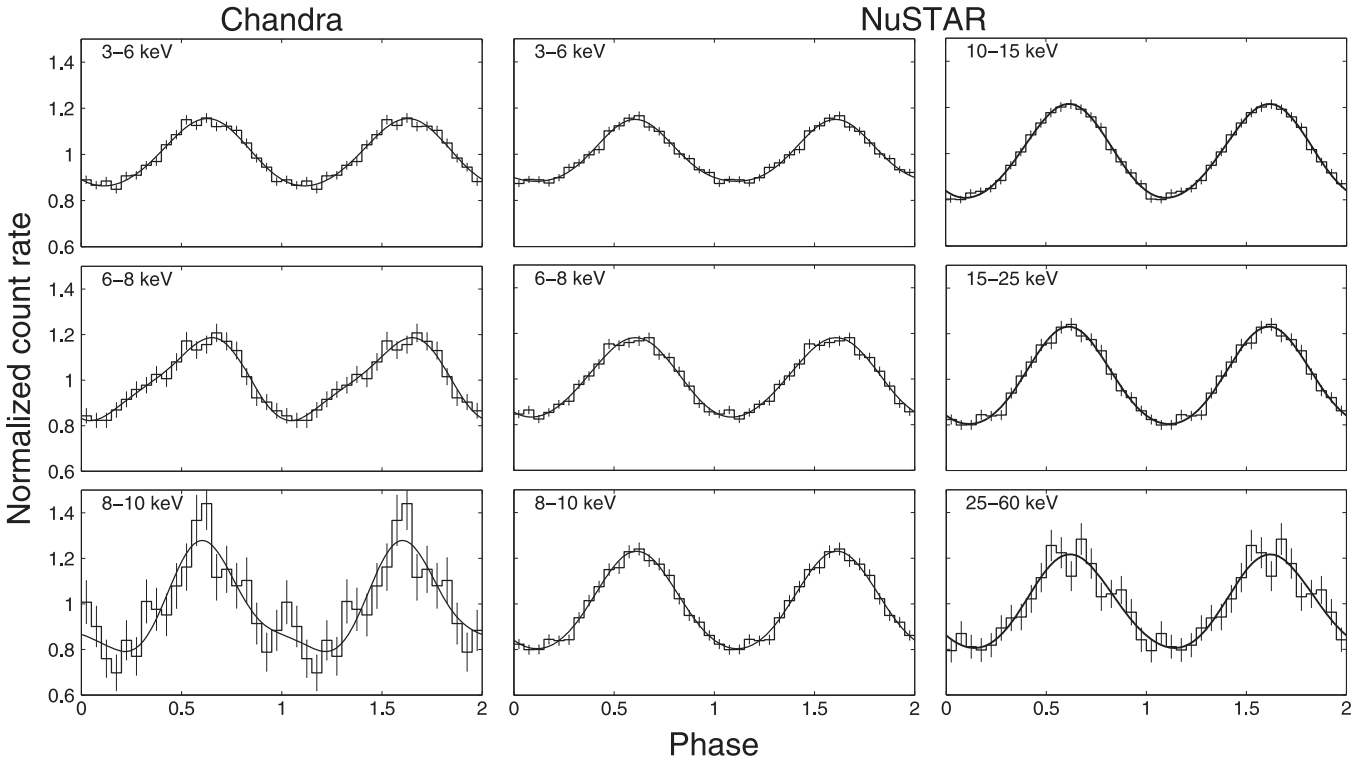

Figure 6. Persistent emission pulse profiles in different energy bands as measured with *Chandra* (*left column*) and *NuSTAR* (*middle and right columns*). The black solid lines are the best-fit models at the pulse period of GRO J1744-28.

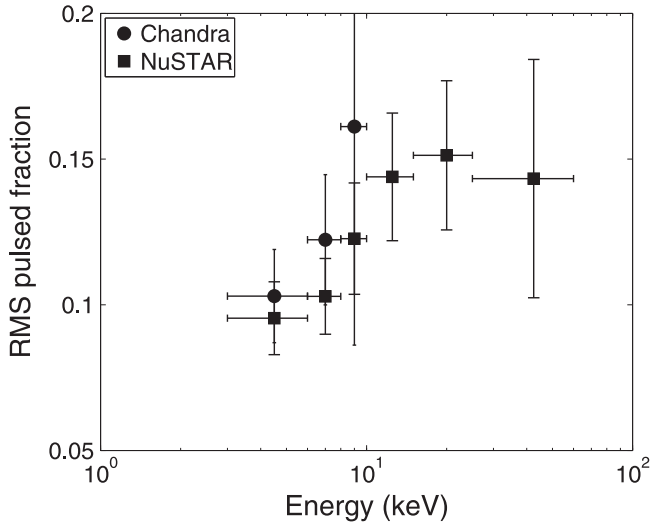

Figure 7. Persistent emission pulse fraction as a function of energy for *NuSTAR* (squares) and *Chandra* (circles).

functions. The PP is nearly sinusoidal. The second harmonic contribution is highest in between 8 and 10 keV ($19\% \pm 10\%$) for *Chandra* and between 6 and 8 keV ($8\% \pm 1\%$) for *NuSTAR*.

The rms pulsed fraction (PF) is defined as (Bildsten et al. 1997)

$$\mathrm{PF}_{\mathrm{rms}} = \frac{\left[0.5\sum_{k=1}^{m}\left(A_k^2 + B_k^2\right) - \left(\sigma_{A,k}^2 + \sigma_{B,k}^2\right)\right]^{0.5}}{C_{\mathrm{mean}}}, \quad (5)$$

where $\sigma_{A,k}$ and $\sigma_{B,k}$ are the 1σ standard deviations on the model coefficients.

We calculate the PF of the persistent emission PPs in different energy bands and find a slight energy dependence in both *Chandra* and *NuSTAR* data. At the lowest energies, 3–6 keV, the PF is about 10%. It increases to 15% in the 10–15 keV energy range and remains constant at higher energies (Figure 7). We find the same dependence and PF values during the dip intervals in both *Chandra* and *NuSTAR*.

We do not perform timing analysis on the burst intervals. Both *Chandra* and *NuSTAR* suffer high instrumental dead-time during bursts, and *Chandra* data suffer a small pileup percentage at the peak of the bursts (10%), all of which distorts the burst PP.

3.3. Spectral Analysis

We perform our spectral analysis using XSPEC (Arnaud 1996) version 12.8.1. The photoelectric cross sections of Verner et al. (1996) and the abundances of Wilms et al. (2000) are used throughout to account for absorption by neutral gas. All quoted uncertainties are at the 1σ level, unless otherwise noted.

3.3.1. Persistent Emission

We extract the HEG m1 spectrum of the persistent emission intervals as defined in Section 3.1 and fit it (binned to a signal-to-noise ratio (S/N) of 10) with an absorbed PL. Residuals in the form of narrow emission lines are present in the spectra in the energy range 6.0–7.5 keV (Figure 8).

To properly model the continuum, we ignore data in the energy range 6.0–8.0 keV. The absorbed PL provides a good fit to the data with a reduced χ^2 of 0.7 for 247 degrees of freedom

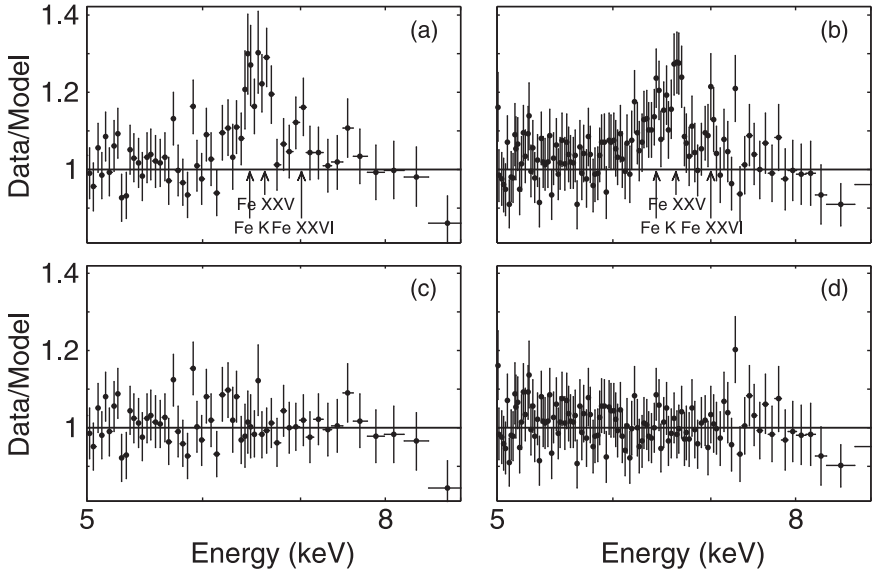

Figure 8. Panel (a) Data to model ratio of a PL fit to the *Chandra* persistent emission spectrum.Panel (b) Data to model ratio of a PL fit to the *Chandra* dips+persistent emission spectrum. In both panels, we ignore the 6.0–8.0 keV range in the fits. Panel (c) Data to model ratio of a PL and three Gaussian lines to the persistent emission spectrum.Panel (d) Data to model ratio of a PL and three Gaussian lines to the dips+persistent emission spectrum. The arrows at the Gaussian centroid energies indicate their possible identification. Data are rebinned for clarity.

Table 3
Chandra HEG m1 Best-fit Parameters for the Dip, Persistent, and Dip +Persistent Emission Intervals

	Persistent	Dips	Dips+Persistent
$N_{\rm H}(10^{22}\ {\rm cm}^{-2})$	8.8 ± 0.3	$9.0^{+0.5}_{-0.4}$	8.9 ± 0.2
Γ	$1.16^{+0.03}_{-0.05}$	1.2 ± 0.1	$1.17^{+0.03}_{-0.04}$
Norm.[a]	$1.01^{+0.07}_{-0.08}$	$0.95^{+0.2}_{-0.1}$	$0.96^{+0.04}_{-0.05}$
$F_{\rm PL}\ (10^{-8})$[b]	$1.22^{+0.02}_{-0.03}$	$1.05^{+0.02}_{-0.03}$	1.15 ± 0.02
E_1 (keV)	$6.45^{+0.06}_{-0.03}$	$6.4^{+0.1}_{-0.2}$	6.44 ± 0.06
σ_1 (eV)	45^{+95}_{-17}	700^{+300}_{-400}	250^{+90}_{-70}
$\rm EW_1$ (eV)	31 ± 14	220^{+140}_{-100}	81 ± 21
$F_1\ (10^{-11})$[b]	$4.0^{+5.0}_{-1.3}$	17^{+10}_{-12}	9.0 ± 2.0
E_2 (keV)	$6.63^{+0.03}_{-0.02}$	$6.66^{+0.03}_{-0.04}$	$6.65^{+0.01}_{-0.02}$
σ_2 (eV)	55^{+21}_{-25}	42^{+42}_{-26}	33^{+15}_{-13}
$\rm EW_2$ (eV)	42^{+17}_{-15}	17^{+12}_{-10}	17^{+8}_{-6}
$F_2\ (10^{-11})$[b]	$5.3^{+1.4}_{-2.3}$	$1.9^{+1.4}_{-0.7}$	2.2 ± 0.8
E_3 (keV)	7.00 ± 0.03	$6.98^{+0.03}_{-0.04}$	6.99 ± 0.02
σ_3 (eV)	68^{+68}_{-34}	11^{+39}_{-11}	32^{+30}_{-16}
$\rm EW_3$ (eV)	25^{+11}_{-13}	10^{+12}_{-10}	15^{+8}_{-7}
$F_3\ (10^{-11})$[b]	$3.0^{+1.7}_{-1.4}$	$0.9^{+0.9}_{-0.7}$	$1.7^{+0.9}_{-0.5}$
$F_{\rm tot}\ (10^{-8})$[bc]	1.23 ± 0.02	$1.08^{+0.02}_{-0.03}$	1.16 ± 0.02

[a] In units of photons $\rm keV^{-1}\ cm^{-2}\ s^{-1}$.
[b] In units of erg $\rm cm^{-2}\ s^{-1}$.
[c] Total unabsorbed flux. $F_{\rm PL}$ and $F_{\rm tot}$ are caclualted in the 0.5–70 keV energy range. Fluxes of the Gaussian components are in the 6–8 keV range.

(dof). We also fit the continuum with a BB function (bbody in XSPEC, BB hereafter), and although we find a statistically acceptable fit with a reduced χ^2 of 0.9, significant fit residuals at low and high energies (<3 and >8 keV) are present. A diskbb model gives as good a fit as the PL with a reduced χ^2 of 0.76; however, the temperature $T_{\rm in} \approx 6.0$ keV of the inner disk is too high for an accreting pulsar. We conclude that a simple PL is sufficient to explain the *Chandra* data alone.

We add the 6.0–8.0 keV data, including three Gaussian lines at 6.4, 6.65, and 7.0 keV to account for the residuals, and re-fit. We find a reduced χ^2 of 0.7 for 291 dof (Figure 8). Table 3 lists the best-fit parameters to the persistent emission continuum and features, along with their 1σ uncertainties. The addition of the 6.4, 6.65, and 7.0 keV Gaussian components (one at a time) improves the fit by a $\Delta\chi^2$ of 24, 31, and 10, respectively. We find that all three lines are narrow with comparable fluxes and equivalent widths (EWs) within uncertainties. Most likely the lines are due to neutral or near-neutral Fe and highly ionized Fe XXV (He-like) and Fe XXVI (H-like). We note here that there is a CCD gap in the HEG m1 at 6.3 keV, right below the energy of the 6.4 keV Fe feature, resulting in loss of counts at that energy, which renders the fit parameters of this line uncertain.

Next, we extract the *NuSTAR* FPMA and FPMB spectra, in the 3–70 keV range for the persistent intervals simultaneous with *Chandra*, and group them to have an S/N of 25. We fit the *NuSTAR* spectra and the HEG m1 spectrum simultaneously, including a normalization factor to all model fits to take into account any cross-calibration uncertainties between the three instruments. We link all fit parameters between the three spectra except for the normalization factor. Both *NuSTAR* spectra show a broad emission line centered at around 6.65 keV, most likely corresponding to the Fe line complex detected with *Chandra*. Hence, for our initial fits, we exclude from both *Chandra* and *NuSTAR* the 6.0–8.0 keV energy range. A single-component model, i.e., PL or BB, does not give a satisfactory fit with a reduced $\chi^2 > 2$. An absorbed *cutoffPL* (a PL with an exponential rolloff) model gives a better fit, but it is also statistically unacceptable (reduced $\chi^2 = 1.8$). The addition of a BB model improves the fit dramatically with a reduced $\chi^2 = 1.3$ (Figure 9, panel (e)). However, this model results in an absorption hydrogen column density three times lower than

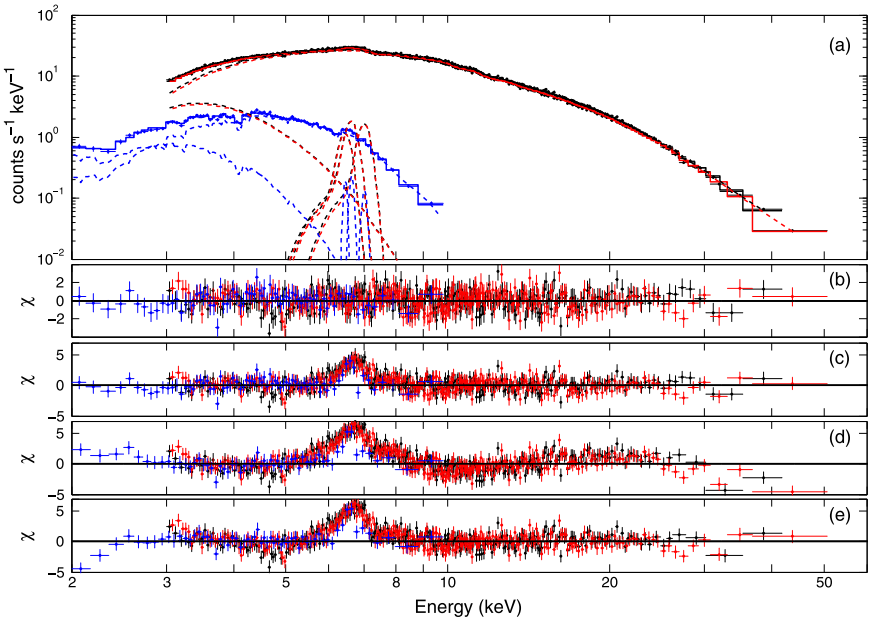

Figure 9. (a) Best-fit model to the *NuSTAR* and *Chandra*/HEG m1 spectra of the persistent emission interval. The model consists of a BB, three Gaussians, a 10 keV feature modeled as *cyclabs*, and a *cutoffPL*, all modified by absorption. A constant normalization is also included for instrument cross-calibration uncertainties. Dashed lines represent the different additive components. (b) Residuals of the data from the best-fit model. (c) Ignoring the 6.0–8.0 keV data and excluding the three Gaussian lines. (d) Excluding the 10 keV feature, and fixing $N_{\rm H}$ to the *Chandra* value. (e) Letting $N_{\rm H}$ free to vary. Data have been refit in panels (c), (d), and (e); in all five panels, the black, red, and blue points are the *NuSTAR* module A, module B, and the *Chandra* HEG m1 data, respectively. *Chandra* data in the bottom two panels are binned-up for clarity. See text for more details.

what we get from *Chandra* alone, resulting in large residuals at the lower end of the spectrum, along with residuals at 10 keV. Hence, we fix $N_{\rm H}$ to the *Chandra* value of 9.0×10^{22} cm^{-2}. This gives a similar fit quality compared to the above, but emphasizes the residuals around 10 keV in the form of a broad trough (Figure 9, panel (d)). Adding a negative broad feature (*cyclabs*[23] in XSPEC) to the model and thawing $N_{\rm H}$ results in the best fit to the continuum with a reduced χ^2 of 0.95 (for 767 dof).

We also investigate the effect of other model continua on the presence and shape of the 10 keV feature. First, instead of a *cutoffpl* model, we fit the spectrum using (1) a Fermi–Dirac form of cutoff (*fdcut*; Tanaka 1986) and (2) a negative–positive PL exponential (*npex*; Mihara 1995), both used for fitting accreting X-ray pulsar spectra. Neither model, modified by absorption, gives a good fit to the data (reduced $\chi^2 \approx 1.9$). Adding a BB results in a reduced χ^2 of 1.3. We then remove the BB component and add a negative broad feature to the models. Both *fdcut* and *npex* give a reduced χ^2 of 1.1 but fail to reproduce the soft part of the spectrum. Adding both a BB component and a negative feature gives a good fit to the data in both cases (reduced χ^2 of 0.94 and 0.95 for 765 and 766 dof for *npex* and *fdcut*, respectively). We conclude that the 10 keV feature and the BB component are present in the data regardless of the shape of the continuum used. We therefore adopt the simplest empirical model, i.e., *cutoffPL*, for the rest of our analysis since it has less free parameters than the above two for comparable fit results. Moreover, the parameters of the BB component and the 10 keV feature are consistent within 1σ in all three models.

Finally, using the *cutoffPL* continuum model, we add the 6.0–8.0 keV data. We include three Gaussian lines with centroid energies and widths fixed to the values derived from the *Chandra* data (reduced χ^2 of 0.91 for 919 dof). We also fit one Gaussian line to the data, with all parameters left free to vary. We find a line centroid energy $E = 6.69 \pm 0.03$ keV and a width $\sigma = 0.42^{+0.06}_{-0.04}$ keV (reduced χ^2 of 0.92 for 919 dof).

We conclude that our best-fit model for the *NuSTAR* and HEG m1 persistent emission spectra consists of a BB, a *cutoffPL*, a 10 keV feature, three Gaussian lines with centroid energies and widths fixed to the *Chandra*-alone values (or one Gaussian component with all parameters left free to vary), all affected by neutral absorption (*tbabs* in XSPEC) and a constant normalization. Table 4 gives the best-fit parameters.

3.3.2. Dips

We extract the *Chandra* HEG m1 spectra for each of the dip intervals separately (here we define the duration of a dip interval as starting from the end of a burst until the time it recovers to 95% of the persistent level). We fit all seven intervals simultaneously with an absorbed PL model. The hydrogen column density is linked for all spectra to ensure that they are all equally absorbed. First, we allow the PL indices and normalizations to vary, and we find that the PL index is consistent across all spectra. Therefore, we also keep the indices linked. We do not find any flux variability between the different dips, and we estimate an average flux and 1σ standard deviation of $(1.05 \pm 0.04) \times 10^{-8}$ erg s^{-1} cm^{-2}. We also find no variability in the fluence deficiency during the different dips (the actual deficit of fluence from the persistent emission during a dip) with an average of $(1.2 \pm 0.2) \times 10^{-6}$ erg cm^{-2}.

[23] We tried three different negative broad components to model the 10 keV feature, *cyclabs*, *gabs*, and an additive Gaussian component with negative normalization. *cyclabs* gives a slightly better fit than the other two with $\Delta\chi^2 = 24$ for the same number of dof. Hence, we use *cyclabs* in the rest of the analysis.

Table 4
Best-fit Parameters for the Dip, Persistent, Dip+Persistent, and Burst Emission Intervals for the Combined *NuSTAR* +*Chandra* Data

	Persistent	Dips	Dips+Persistent	Bursts
$N_{\rm H}$ (10^{22} cm^{-2})	11.2 ± 0.7	9.7 ± 1.0	10.6 ± 0.6	7.3 ± 0.7
$kT_{\rm BB}$	0.55 ± 0.03	0.52 ± 0.03	0.52 ± 0.02	…
Norm.$_{\rm BB}$ (10^{-2})[a]	$4.0^{+1.0}_{-0.8}$	$4.6^{+1.5}_{-1.2}$	$4.1^{+0.8}_{-0.7}$	…
$F_{\rm BB}$ (10^{-9})[b]	4.5 ± 0.6	4.3 ± 0.8	$4.5^{+0.4}_{-0.5}$	…
E_1^d (keV)	6.45	6.4	6.44	…
σ_1^d (eV)	45	700	250	…
EW$_1$ (eV)	22^{+8}_{-5}	141^{+36}_{-33}	47^{+5}_{-7}	…
F_1 (10^{-11})[b]	2.9 ± 0.8	12 ± 2	5.5 ± 0.7	…
E_2^d (keV)	6.63	6.66	6.65	…
σ_2^d (eV)	55	42	33	…
EW$_2$ (eV)	33^{+7}_{-5}	27^{+6}_{-4}	22 ± 3	…
F_2 (10^{-11})[b]	$4.5^{+0.5}_{-0.6}$	$3.2^{+0.6}_{-0.5}$	3.2 ± 0.5	…
E_3^d (keV)	7.01	6.98	6.99	…
σ_3^d (eV)	68	11	32	…
EW$_3$ (eV)	36^{+6}_{-4}	15^{+4}_{-5}	27^{+2}_{-3}	…
F_3 (10^{-11})[b]	$4.5^{+0.5}_{-0.4}$	1.7 ± 0.4	3.6 ± 0.3	…
E_b (keV)[c]	6.69 ± 0.03	6.71 ± 0.04	$6.70^{+0.02}_{-0.03}$	…
σ_b (eV)	400^{+60}_{-40}	420 ± 50	420^{+40}_{-20}	…
EW$_b$ (eV)	123^{+16}_{-12}	133^{+9}_{-13}	129^{+10}_{-9}	…
F_b (10^{-11})[b]	15^{+2}_{-1}	14^{+2}_{-1}	15 ± 1	…
$E_{10\,\rm keV}$ (keV)	9.9 ± 0.2	$9.5^{+0.3}_{-0.4}$	9.9 ± 0.1	10.5 ± 0.3
$\sigma_{10\,\rm keV}$ (keV)	$3.7 \pm^{+0.4}_{-0.3}$	$4.2^{+0.6}_{-0.5}$	$3.6^{+0.3}_{-0.2}$	$0.8^{+0.8}_{-0.3}$
$d_{10\,\rm keV}$	0.16 ± 0.02	0.18 ± 0.02	0.17 ± 0.01	0.15 ± 0.04
Γ	$0.0^{+0.2}_{-0.1}$	0.0 ± 0.1	0.00 ± 0.04	0.2 ± 0.1
$E_{\rm fold}$	7.0 ± 0.2	7.0 ± 0.2	7.1 ± 0.1	7.6 ± 0.5
Norm[a]	$0.29^{+0.03}_{-0.02}$	0.26 ± 0.03	0.30 ± 0.02	$1.9^{+0.3}_{-0.2}$
$F_{\rm PL}$ (10^{-8})[b]	2.49 ± 0.04	$2.24^{+0.06}_{-0.05}$	2.37 ± 0.03	9.8 ± 0.2
$F_{\rm tot}$ (10^{-8})[be]	2.62 ± 0.02	$2.30^{+0.03}_{-0.02}$	2.47 ± 0.01	$8.9^{+0.2}_{-0.1}$

[a] In units of photons keV^{-1} cm^{-2} s^{-1}.
[b] In units of erg cm^{-12} s^{-1}.
[c] Fitting one Gaussian line to the Fe line complex.
[d] Fixed to the *Chandra* best-fit results.
[e] Total unabsorbed flux. $F_{\rm BB}$, $F_{\rm PL}$, and $F_{\rm tot}$ are caclualted in the 0.5–70 keV energy range. Fluxes of the Gaussian components are in the 6–8 keV range.

Table 2 gives the spectral results for the individual dip intervals.

Motivated by the differences in the count rates at the dip minima (Figure 5), we extract the HEG m1 spectra of all seven dips in an 80 s interval centered at $t_{\rm min}$ and fit them simultaneously with an absorbed PL model, keeping only the normalizations free. We do not find any flux variability (at the $>3\sigma$ level) in the minimum level the dips reach after each burst (Table 2). We repeat the analysis for a 40 s interval centered at $t_{\rm min}$ and reach the same conclusions.

Next, we extract the HEG m1 spectrum for dip intervals *collectively* and group them so that each bin has an S/N of 10. We fit the spectrum with an absorbed PL and find an absorption hydrogen column density and a PL index consistent within errors with the results we find for the persistent emission intervals (Table 3). We find an unabsorbed average flux $F = 1.05^{+0.02}_{-0.03} \times 10^{-8}$ erg s^{-1} cm^{-2}. The ratio of the average flux (over the entire dip intervals) to the persistent emission flux is 0.86, or a 14% drop in the persistent emission flux.

Finally, we find that some residuals are present in the HEG m1 at high energies (>6 keV), in the form of excess emission, similar to what is seen in the persistent emission spectrum. Hence, we add three Gaussian lines at 6.4, 6.65, and 7.0 keV. Table 3 lists the best-fit parameters to the dip intervals. Unfortunately, due to the low number of counts in the dip spectra, we are not able to adequately constrain the parameters of the Gaussian components, except for their energies. Nonetheless, comparing the dip and persistent emission fit parameters, we do not find dramatic changes in the line properties. These results are discussed in Section 4.

We then apply the same model we used to fit the persistent interval *Chandra+NuSTAR* broadband spectrum to the dip broadband spectrum. We find very similar values between persistent and dip intervals, except for the flux of the *cutoffPL*

component, which decreased by 10% during dips. The fluxes of the BB and the Fe line component (considering one Gaussian line fit to the 6.7 keV excess) did not change within their 1σ error. These results are shown in Table 4.

3.3.3. Persistent Emission and Dips

To achieve better S/N for the spectral fitting of the lines, we extract the HEG m1 spectrum of the persistent and dip intervals together. We fit the spectrum with an absorbed PL model and three Gaussian emission lines (Figure 8). Table 3 lists the best-fit parameters along with their 1σ uncertainties.

According to the persistent+dip spectrum, which has better statistics than the persistent or dip spectra alone, the highly ionized lines are narrow with widths of about 30 eV. They also contribute similarly to the total flux. The neutral Fe, on the other hand, has a larger width and flux compared to the other two.

The broadband model used to fit the persistent and dip spectra alone is also successfully fit to the dips+persistent *NuSTAR* and *Chandra* spectra (Table 4). All the parameters of the best-fit model were compatible with the persistent and dip fits. A one-Gaussian emission-line fit to the 6.7 keV excess results in a width $\sigma = 0.42$ keV and an EW = 129 eV. Finally, we also fit the 6.7 keV excess using a diskline model (Fabian et al. 1989) and find $E = 6.63^{+0.05}_{-0.04}$ keV, $R_{\rm in} = 130^{+240}_{-80}$ GM/c^2 ($3^{+5}_{-2} \times 10^7$ cm), and $i > 35°$ (all quoted uncertainties are at the 3σ level).

3.3.4. Bursts

We extract the HEG 1 spectrum for each of the seven bursts seen with *Chandra* and fit them simultaneously with an absorbed PL. We link the hydrogen column density in the fit. We find a consistent PL index for all spectra, and therefore, we also link the index thereafter. The PL normalizations are left free to vary, to account for any flux variability between the bursts. We find $N_{\rm H} = (9.0 \pm 1.0) \times 10^{22}$ cm^{-2} and a PL index of $\Gamma = 1.2 \pm 0.2$. We report in Table 1 all burst spectral parameters.

We find very similar energetics between the different bursts; flux and luminosity variability (at the 3σ level) is observed only between bursts #4 and #7 (these are the shortest and the longest burst, respectively; Table 1). In terms of fluence, all bursts emitted comparable (at the 2σ level) amounts of energy. The mean and 1σ standard deviation of the fluxes and fluences are $(7.4 \pm 1.6) \times 10^{-8}$ and $(10.3 \pm 1.6) \times 10^{-7}$ erg cm^{-2}, respectively. We also convert the 1 s peak count rates of the seven bursts to fluxes using PIMMS (due to the low count statistics). We find an average peak flux of 2.0×10^{-7} erg s^{-1} cm^{-2}, equivalent to a luminosity of 1.5×10^{39} erg s^{-1} at 8 kpc. This value should be regarded as a lower limit due to a 10% pileup and the narrow energy band for which it was derived (0.5–10 keV; *NuSTAR* data were excluded from this analysis due to severe dead-time effects).

We extract the HEG 1 spectrum of all seven bursts collectively, grouped to an S/N of 7, to search for any features present in their added spectrum. We fit the spectrum with an absorbed PL and find a hydrogen column density $N_{\rm H} = (1.0 \pm 0.1) \times 10^{23}$ cm^{-2} and a PL index $\Gamma = 1.2 \pm 0.1$. No prominent absorption and/or emission features are seen in the spectrum.

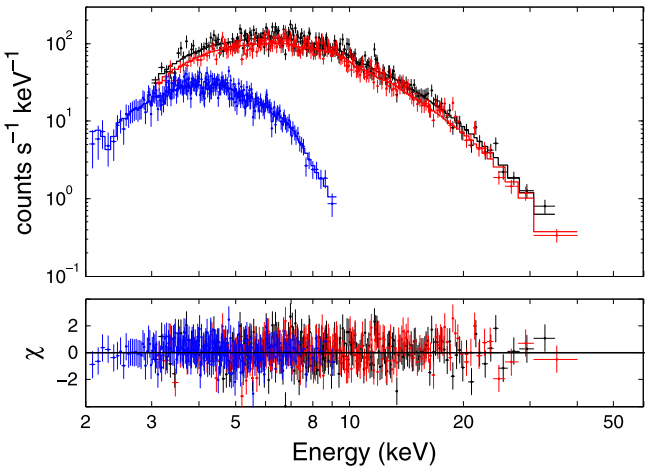

Figure 10. Upper panel: Data and best-fit model to the *Chandra+NuSTAR* burst spectra. The model consists of a *cutoffPL* and a 10 keV feature, modified by absorption. Lower panel: Deviations from the fit in terms of sigmas. Black, red, and blue points are the *NuSTAR* module A, module B, and the *Chandra* HEG m1 data, respectively.

We then extract the 3–70 keV *NuSTAR* spectrum of the three bursts seen simultaneously with *Chandra*, binned to an S/N of 15. We fit the spectrum with an absorbed *cutoffPL* resulting in a reduced χ^2 of 0.89 for 637 dof. Some residuals around 10 keV can be seen, similar to what we find in the persistent and dip spectra. Including a *cyclabs* feature to the model improved the fit slightly, resulting in a reduced χ^2 of 0.86 for 634 dof, which is a $\Delta\chi^2$ of 17 for three additional parameters. Figure 10 shows the data and best-fit model, while the parameter values are listed in Table 3. We see no excess emission between 6 and 8 keV. We derive a 3σ upper limit of 119 eV on the EW of a line with centroid energy at 6.7 keV. We also derive a 3σ upper limit on the flux of a line at the same energy and a width of 0.4 keV of 1.4×10^{-10} erg s^{-1} cm^{-2}. Using the co-added *Chandra* burst spectra, we derive a 30 eV 3σ upper limit on the EW of the neutral Fe and 16 eV on the highly ionized species. Assuming a width of 0.05 keV for the Fe K and the highly ionized species, we find 3σ flux upper limits of the order of 10^{-10} erg s^{-1} cm^{-2} for all three lines. These upper limits indicate that if any of the lines we detect in the dip and persistent spectra brightened proportionally to the burst flux (on the average by a factor of 5), we should have been able to detect them. However, if the line fluxes remained constant during the bursts, their presence could be masked by the much brighter burst continuum.

Finally, we note that the BB component is not required by the fit to the burst's spectrum at a high significance. However, the hydrogen column density is lower at the 3σ level than the value derived for the dips and persistent intervals (Table 4). Hence, fixing the column density at 10.6×10^{22} cm^{-2}, we find residuals at the lower end of the spectrum, which are well fit with a BB component with $kT \approx 0.6$ keV and a 0.5–70 keV flux of $(3 \pm 2) \times 10^{-9}$ erg s^{-1} cm^{-2}, consistent with the BB temperatures and fluxes during the persistent and dip intervals. These results are discussed in Section 4.2.

3.4. Phase-resolved Spectroscopy

We divide the broadband persistent emission spectrum into five pulse phase bins, which we fit simultaneously with our best-fit model described above. We fit the 6.7 keV excess

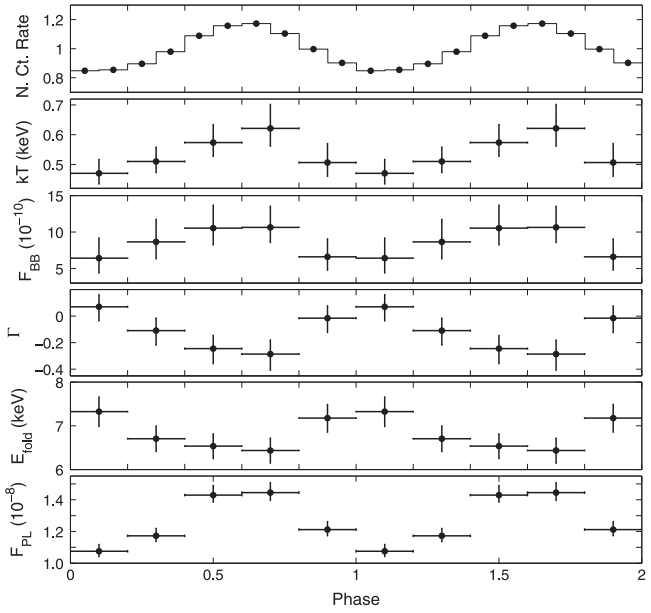

Figure 11. Broadband phase-resolved spectroscopy during the persistent emission of the BP. From top to bottom, PP in the 3–70 keV range, BB temperature, BB flux, *cutoffPL* index, energy roll-off, and *cutoffPL* flux. See text for more details.

energy with one Gaussian line. We first leave all model parameters free to vary. We link one model parameter after another (starting from the least variable according to a χ^2 test) and record the F-test significance at each step to assess the significance of leaving the parameter free in the fit. We find that the fit parameters of the 6.7 and 10 keV features do not show significant changes with pulse phase. On the other hand, the BB and *cutoffPL* fit parameters tightly follow the PP shape (Figure 11). We find a decrease in the photon index Γ and an increase in the BB temperature, indicating that the X-ray spectrum hardens at pulse maximum. The roll-off energy is also anti-correlated with the pulse shape.

4. DISCUSSION

4.1. Burst and Dip Origin

Our temporal analysis shows that six out of the seven detected bursts have comparable durations with an average of about 12 s. These consist of a single pulse with a faster rise than decay time. The seventh burst detected by *Chandra* is the only outlier with a duration of about 25 s, consisting of two pulses. These temporal properties are similar to the properties of hundreds of bursts recorded during the first two outbursts from the BP (e.g., Woods et al. 1999).

From the *Chandra* data, we can derive the α parameter, the ratio of the fluence in the persistent emission to the fluence in the bursts. We find $\alpha < 15$ for all bursts (except for the sixth one where $\alpha = 30$), with an average value of 10. The same value was also derived during the first two outbursts from the source (Mejía et al. 2002). As pointed out by Lewin et al. (1996), this small value of α is inconsistent with thermonuclear burning as the origin for the BP bursts. This value is consistent with the observed bursts being type II bursts, similar to what is seen in the Rapid Burster, caused by some sort of instability associated with the accretion disk (Lamb et al. 1977; Baan 1979; Taam & Lin 1984; Lasota & Pelat 1991; Spruit & Taam 1993; Cannizzo 1996; D'Angelo & Spruit 2010). Unlike the Rapid Burster, however, the BP does not display any correlation between the fluence in a burst and the time to the following burst (e.g., Kouveliotou et al. 1996). This is also evidenced by our data, where the fluence emitted during all seven bursts is constant while the intervals between bursts changed by up to a factor of 4.

Similar to the previous two outbursts, the bursts we detect in *Chandra* and *NuSTAR* are followed by a dip, where the X-ray emission decreases by 10% on average and 40% at dip minimum. The emission exponentially recovers back to the pre-burst persistent level, on timescales of a few hundred seconds. We find that the fluence in a burst and the integrated flux deficiency of the following dip are consistent within 1σ (Tables 1 and 2). We estimate an average burst fluence (2–10 keV) of $(1.0 \pm 0.2) \times 10^{-5}$ erg cm^{-2} and an average *missing* dip fluence of $(1.2 \pm 0.2) \times 10^{-5}$ erg cm^{-2}. Such a correlation was also seen during the previous two outbursts (e.g., Nishiuchi et al. 1999). These authors suggested that the energy emitted during a burst could be compensated by the deficit in energy during the following dip. A very simple picture would be that accretion-disk instabilities would allow for a sudden and rapid increase of the mass-inflow rate onto the polar cap of the neutron star from a reservoir (e.g., the accretion disk). The dips, then, would be the result of a small fraction of the continuously accreted matter disappearing to replenish this reservoir.

4.2. X-ray Emission Properties

The broadband spectrum of the BP is the typical spectrum of an accreting X-ray pulsar at high accretion rates (see e.g., Coburn et al. 2002, for a review). It is well fit with a hard component, modeled as a PL with an exponential roll-off, an Fe line complex, a soft component modeled with a BB, and a 10 keV feature, all modified by absorption. In the following, we will discuss these different components and their interplay between persistent, dip, and burst emission, except for the Fe line complex, which is discussed in Section 4.3.

The high persistent X-ray luminosity of GRO J1744-28 during the present observation ($L_X = 1.9 \times 10^{38}$ erg s^{-1}) implies that the emission is coming from an accretion column, where the kinetic energy of the infalling gas onto the polar cap is converted to radiation via a radiative shock above the thermal mound (Basko & Sunyaev 1975). Thermal photons from the mound, as well as cyclotron and bremsstrahlung radiation, are converted to high-energy photons via inverse Compton scattering. Hence, the resulting X-ray spectrum will depend on several parameters such as the geometry of the system and the properties of the compact source—mainly its dipole magnetic field—among others (Becker & Wolff 2007). Even with the small dipole magnetic field of GRO J1744-28 and its complicated accretion geometry (Miller 1996), the parameters we derive from our phenomenological fit compare reasonably well to other accreting X-ray pulsars (e.g., Suchy et al. 2011; DeCesar et al. 2013; Müller et al. 2013; Fürst et al. 2014b). The photon index of the *cutoffPL* is slightly lower than in most cases, implying a harder spectrum, which could be the result of the higher luminosity of the source. Simply put, a higher accretion rate onto the poles would lead to a higher electron density in the accretion column and to higher Compton y-parameter, causing a harder spectrum. The GRO J1744-28 spectrum also shows a lower energy roll-off compared to

other sources, which could be due to the relatively low magnetic field of the source (Coburn et al. 2002).

The 10 keV feature is not unique to GRO J1744-28 and has previously been reported in other accreting X-ray pulsars, e.g., Vela X-1 (Müller et al. 2012; Fürst et al. 2013, 2014a; see also Coburn et al. 2002 for a review). This feature is not always necessarily observed as an absorption trough and sometimes manifests itself as a broad emission feature or a wiggle. It is believed to be the result of modeling accreting X-ray pulsar spectra with simple empirical functions, when the true physics giving rise to their X-ray spectra is far more complicated, especially when they are emitting near the Eddington limit (see Coburn et al. 2002, for a discussion). In a few cases, however, such as in the case of the Be/X-ray binary *Swift* J1626.6-5156 (DeCesar et al. 2013), an absorption line at 10 keV was interpreted as a cyclotron resonance scattering feature (CRSF), evidenced by the presence of a weak second harmonic and the fact that the B field strength, derived from the line energy, was consistent to the value derived from the spin-up rate of the source (Içdem et al. 2011). In the 10 ks of *NuSTAR* data that we consider here, we find no evidence of a second harmonic at about twice the energy of the 10 keV feature (i.e., 20 keV), and the B field strength corresponding to the line energy ($B \approx 9 \times 10^{11}$ G for a 10 keV line energy) is significantly larger than the estimates we derive in Section 4.4. Moreover, CRSFs usually show strong dependence with pulse phase (e.g., Fürst et al. 2014b), which we do not observe in our phase-resolved spectroscopy. Hence, we consider the 10 keV feature in GRO J1744-28 spectrum to be a defect of our continuum modeling. We note, however, that unlike the BP, other X-ray pulsars showing 10 keV features invariably show CRSFs.

Soft excess emission is often modeled with a BB component in accreting X-ray pulsars. Hickox et al. (2004; see also Ballantyne et al. 2012) showed that in luminous sources such as GRO J1744-28, the most likely source for this BB-like emission is the inner region of the accretion disk, from where the reprocessed hard X-ray emission of the accretion column is emitted. Such reprocessed emission also pulsates at the pulse period of the hard X-ray component, most likely with a lower PF due to the large area where the reprocessing is taking place. This is in agreement with both the change of the BB temperature and flux with pulse phase (Figure 11) and the slight decrease of the PF at low energies compared to the high energies (Figure 7). Under this assumption and for isotropic emission, the inner radius of the disk is $R_{\rm BB}^2 = L_{\rm X}/(4\pi\sigma T^4)$ (Hickox et al. 2004), where σ is the Stefan–Boltzmann constant, $L_{\rm X}$ is the non-thermal X-ray luminosity, and T is the BB temperature in K. The temperature we calculate, however, is the apparent temperature of the plasma and is related to the effective temperature through a color-correction (or hardness) factor, $f_{\rm c} = T_{\rm c}/T_{\rm eff}$ (Damen et al. 1990; Shimura & Takahara 1995; Li et al. 2005), which is usually taken to be between 1.5 and 2. Hence, the true inner radius of the BB emission area is $R_{\rm in} = f_{\rm c}^2 R_{\rm BB}$ (Kubota et al. 1998). We find $R_{\rm in} = (4 \pm 1) \times 10^7$ cm (3σ confidence), for $f_{\rm c} = 1.8$. This is consistent with the expected small accretion disk radius considering the low B field of the source and its high luminosity.

The burst broadband spectrum requires only emission from the non-thermal component, with fit parameters similar to the ones we derive for the persistent emission. This reinforces our above picture where we envisioned the burst emission to be the result of a sudden increase of the mass accretion rate onto the neutron-star pole. The non-detection of the BB component implies that the reprocessing of the non-thermal emission may not have taken place during bursts. This is possible, for instance, if the burst emission is anisotropic away from the reprocessing material, i.e., the inner accretion disk. Such anisotropy for the BP has already been discussed by Daumerie et al. (1996) and Nishiuchi et al. (1999) to explain the extremely high luminosities of the bursts during the previous two outbursts, which reached luminosities two orders of magnitude above Eddington. This conclusion is also supported by the timing properties of the source, for which the hard X-ray PF has been seen to increase prominently during the bursts (Stark et al. 1996; Woods et al. 2000).

Finally, the broadband spectrum of the dip intervals is similar to the persistent emission spectrum. The flux deficiency during dips is primarily seen in the non-thermal component, where the *cutoffPL* flux decreased by 10% compared to the persistent emission flux. This is again in agreement with the accretion picture where the dips are essentially the result of a fraction of the long-term accreted matter not reaching the neutron star pole, instead replacing the matter that produced the preceding burst.

4.3. The Fe Line Complex

The ASCA observations during the first outburst of GRO J1744-28 revealed a feature between 6 and 8 keV in its persistent emission spectrum. Nishiuchi et al. (1999) modeled the spectrum with a Gaussian line with a centroid energy of 6.7 keV and an EW of about 300 eV. The line was not resolved by the spectral resolution of ASCA, but its energy is indicative of a blend of emission lines from different species. The *NuSTAR* persistent and dip spectra show a similar emission excess at the same centroid energy and a somewhat smaller EW (although consistent at the 3σ level).

Using the *Chandra* HETGs, we are able to resolve the broad feature into three emission lines, which we identify as Fe K from neutral and/or lowly ionized species at 6.44 ± 0.06 keV and highly ionized Fe XXV and Fe XXVI at $6.65^{+0.01}_{-0.02}$ and 6.99 ± 0.01 keV (these are the best estimates of the line energies from the dip+persistent emission spectrum; see also Degenaar et al. 2014).

We discuss first the Fe emission lines from highly ionized species in the X-ray spectrum of GRO J1744-28. The gas producing the lines is most likely photoionized by the X-ray emission of the neutron star. In photoionized gas, He-like Fe emission lines are produced by recombination and resonant scattering (Matt et al. 1996) and include four different transitions at slightly different energies, the resonant line w, the two inter-combination lines x and y, and the forbidden line z (see, e.g., Porquet & Dubau 2000; Porquet et al. 2010). Here we could not resolve the different resonances; however, from the centroid energy of the Fe XXV line, $6.65^{+0.01}_{-0.02}$ keV, we can safely conclude that the resonant line w (with mean energy at 6.700 keV) contributed minimally to the line strength, and hence the emission is dominated by recombination (Matt et al. 1996; Kallman & Bautista 2001; Bianchi & Matt 2002; Bianchi et al. 2005).

To investigate the origin of the highly ionized species, we simulate XSTAR grids (Bautista & Kallman 2001; Kallman & Bautista 2001) based on the broadband X-ray spectrum of the source. We choose a covering fraction of 0.2 (assuming an

accretion disk) and solar abundances as in Grevesse et al. (1996). Due to the high accretion rate of the source, one would expect the photoionized gas to have a very large density; hence, we examined different values of the gas density n from 10^{10} to 10^{20} cm^{-3}, each time multiplying by 10, to test the effects of density on reproducing the line shapes. We find that the best densities to reproduce the lines, resulting in reasonable values of the ionization parameter ($1 < \log \xi$ (erg cm s^{-1}) < 5), are 10^{15} and 10^{16} cm^{-3}. Here we consider a density of $n = 10^{16}$ cm^{-3}. Finally, we assumed no turbulence in the gas. Fitting this XSTAR simulated grid to the persistent+dip spectrum, we find a best-fit value for the column density in the gas[24] of $N_{\rm H} = 3.4 \times 10^{22}$ cm^{-2} ($<4 \times 10^{23}$ cm^{-2}) and for the ionization parameter $\log \xi$ (erg cm s^{-1}) $= 3.4^{+0.8}_{-0.4}$. The ξ parameter is related to the total X-ray luminosity of the source, L, the density of the ionized gas, n, and its distance from the ionizing source, R, by $\xi = L/nR^2$. Solving for R, we find $R = (2 \pm 1) \times 10^9$ cm (3σ confidence). This distance is similar to the estimates of the ionized gas location in other sources (e.g., Kallman et al. 2003; Jimenez-Garate et al. 2005; Paul et al. 2005; Ji et al. 2009) and points toward reprocessing in an accretion disk corona.

The other interesting feature in our spectra is the (quasi-) neutral Fe at 6.4 keV. There are three possibilities for the formation site of the fluorescence Fe K line in X-ray binaries: (i) a wind from the companion seems to be unlikely in the case of GRO J1744-28, since the companion is a low-mass star and accretion is most likely occurring through Roche-lobe overflow (Finger et al. 1996a); (ii) the companion surface via reflection, which is also hard to achieve, because of the very low inclination of the system (Finger et al. 1996a; Rappaport & Joss 1997), would result in a very low EW for any Fe features (Basko 1978); or (iii) the outer regions of the accretion disk, by means of irradiation from the central source. To test this third possibility, we fit a second XSTAR grid, similar to the one above, to the dips+persistent spectrum. We find that the (quasi-)neutral Fe line is well reproduced with an ionization parameter $\log \xi$ (erg cm s^{-1}) $= 1.6$ (<2.3 at 3σ confidence), much lower than the value required to model the highly ionized lines. This ionization parameter corresponds to a distance from the neutron star of $R = 1.5 \times 10^{10}$ cm ($>7.0 \times 10^9$ cm at 3σ confidence). This seems to point to the outer regions of the accretion disk as the likely origin of the Fe K. Other X-ray binary sources showed, similar to GRO J1744-28, Fe Kα lines most likely from the outer region of an irradiated disk (e.g., Miller et al. 2002; Reynolds & Miller 2010).

The 6.7 keV excess in the simultaneous *NuSTAR* and *Chandra* data is also consistent with a broad line that we fit using a diskline model (see also Degenaar et al. 2014). The inner disk radius that we find ($R_{\rm in} = 3^{+5}_{-2} \times 10^7$ cm) is consistent with the results of Degenaar et al. (2014) and in agreement with a magnetically truncated accretion disk. This radius, however, is more than an order of magnitude smaller than the result we get from the XSTAR fits to the highly ionized lines (assuming that the broad line is consistent with Fe XXV; Degenaar et al. 2014). This could be due to either the uncertainties in the density of the ionizing gas and/or in the distance to the source, or the fact that other broadening mechanisms, e.g., Compton scattering, are contributing to the line profile.

Due to the low statistics of the present observation, we could not constrain any variations in the separate *Chandra* lines during dips (Table 3). The *NuSTAR* Gaussian line fit to the 6.7 keV excess has energy, width, EW, and flux consistent within 1σ between persistent and dip emission (Table 3). The excess emission is not detected during bursts, which means that either the super-Eddington burst X-ray luminosity fully ionized the line-emitting region, including the Fe K region, or the line strength remained more or less constant during bursts, but was masked by the very bright continuum. To explore the first possibility, we simulated the same XSTAR grid as above, but instead of the persistent X-ray luminosity, we used the X-ray luminosity as derived from the bursts. We fit this XSTAR table to the burst spectrum and derived a 3σ lower limit on the ionization parameter $\log \xi$ (erg cm s^{-1}) > 3.0. This limit represents the lowest ionization state that would result in the featureless spectrum that we see during bursts. This lower limit translates into an upper limit on the radius of the ionized material of $R < 8.5 \times 10^9$ cm. Hence, the burst luminosity is capable of fully ionizing the region of the disk where the highly ionized lines are thought to originate ($(2 \pm 1) \times 10^9$ cm). At the 3σ upper limit, it is capable of fully ionizing the region of the neutral Fe ($>7.0 \times 10^9$ cm). This result does not exclude the second possibility.

4.4. Magnetic Field Estimate

Similar to the previous two outbursts from GRO J1744-28, the increase in the X-ray luminosity of the source is accompanied by an increase in the spin period of the neutron star (GBM pulsar team; see footnote 2). This spin-up factor and persistent pulsed emission indicate that the accretion onto the neutron star is not quenched at the disk-magnetosphere boundary, i.e., the propeller effect is not acting. For spin-up to occur during accretion, the inner disk rotational frequency at the magnetospheric radius has to be greater than the neutron star spin frequency, which results in an upper limit on the magnetic dipole field of

$$B < 2\, K^{-7/4} (2\pi\nu)^{-7/6} R^{-5/2} L^{1/2} \left(GM_{\rm NS}\right)^{1/3}, \quad (6)$$

where L is the total X-ray luminosity assuming a distance of 8 kpc, G is the gravitational constant, M and R are the mass and radius of the neutron star, taken to be 1.4 $M_\odot$ and 10 km, ν is the neutron star spin frequency, and K is a dimensionless parameter between 0.5 and 1 (Ghosh & Lamb 1979; Arons 1993; Spruit & Taam 1993; Ostriker & Shu 1995; Finger et al. 1996b; Wang 1996). We find $B < 3.5 \times 10^{11} K^{-7/4}$ G. This value is consistent with the estimates of the previous two outbursts (e.g., Finger et al. 1996a; Bildsten & Brown 1997). We note that the true upper limit is lower than the above derived value since the source started spinning up at earlier stages in the outburst when the source luminosity was lower.

Assuming that the BB component is the result of reprocessing in the inner regions of the accretion disk, we could also use the BB radius estimate (Section 4.2) to derive the strength of the dipole field of the source. The inner accretion disk radius can be written as

$$r_0 = K\, \mu^{4/7} (GM)^{1/7} R^{-2/7} L^{-2/7}, \quad (7)$$

[24] Due to the absence of absorption lines in the spectrum, the column density of the emitting gas could not be well constrained.

with $B = 2\mu R^{-3}$. We find

$$B = 9^{+1}_{-2} \times 10^{10} \left(\frac{K}{1}\right)^{-7/4} \left(\frac{R}{10\ \mathrm{km}}\right)^{-5/2} \times \left(\frac{M}{1.4\ M_{\odot}}\right)^{-1/4} \left(\frac{D}{8\ \mathrm{kpc}}\right) G, \quad (8)$$

which is consistent with the above upper limit and the expected low dipole field of the source.

5. CONCLUSION

We studied the broadband X-ray emission (0.5–70 keV) of the BP from a ≃3 hr simultaneous *NuSTAR–Chandra* observation during its third detected outburst since discovery and after nearly 18 yr of quiescence. These data were taken a few days before the outburst reached its peak.

A total of seven bursts are detected during our observation. Temporal analysis revealed that the first six bursts have comparable shapes, consisting of a single pulse with duration of 12 s and a faster rise than decay time. The last burst has a double-peaked morphology with a duration of about 25 s. All seven bursts, however, have equal fluences with an average of about 10^{-6} erg cm^{-2}. Similar to previous results, we find an average ratio of the burst to the persistent emission fluence $\alpha \approx 10$ (with the exception of one burst where $\alpha = 30$), pointing to the type II origin for the bursts. Each of the seven bursts is followed by a dip in the persistent emission flux, which recovers exponentially with a characteristic timescale $\tau \approx 190$ s. We find an average missing fluence in the dip of about 10^{-6} erg cm^{-2}, consistent with the fluence emitted in the bursts. This indicates that the energy emitted during the burst is compensated for in the dip, and that the long-term accretion rate is constant. The PP of the persistent and the dip intervals are nearly sinusoidal with only weak contribution from the second harmonic. The PF increases from about 10% at 4 keV to 15% at 13 keV and remains constant thereafter.

The BP persistent and dip broadband spectra are identical and well fit with a BB with $kT = 0.5$ keV, a *cutoffPL* with an index $\Gamma = 0.0$ and an energy roll-off $E_{\mathrm{fold}} = 7$ keV, a 10 keV feature assumed to be the result of inadequate modeling of the *cutoffPL*, and a 6.7 keV emission feature, all modified by neutral absorption. Phase-resolved spectroscopy shows that the BB and the *cutoffPL* components show variations at the pulse period of the source, both getting harder at pulse maximum, whereas no significant changes are seen in the 10 keV and the 6.7 keV feature.

Assuming that the BB is reprocessing of the non-thermal emission in the inner regions of the accretion disk, we derive an inner disk radius $R = 4 \times 10^7$ cm. This radius translates into a dipole magnetic field of $B \approx 9 \times 10^{10}$ G.

The *Chandra*/HETG spectrum resolved the 6.7 keV feature into (quasi-)neutral and highly ionized Fe XXV and Fe XXVI narrow emission lines. Modeling the highly ionized lines with XSTAR places the emitting region at a distance of about 10^9 cm from the neutron star, consistent with an accretion disk corona origin. Using a similar XSTAR grid to model the (quasi-)neutral Fe, we find that it originates from a distance $\gtrsim 10^{10}$ cm, most likely the outer regions of an accretion disk.

The broadband burst spectrum, with a peak flux more than an order of magnitude higher than Eddington, is well fit with a *cutoffPL* and a 10 keV feature, with similar fit values compared to the persistent and dip spectra. The burst spectrum, however, lacks a thermal component (BB) and Fe features. If the burst emission were anisotropic (beamed), the lack of the BB component is expected since no reflection of the burst photons on the inner disk would take place. Similarly the Fe XXV, FeXXVI, and the neutral Fe lines would remain at the flux levels detected in the persistent and dip emission and, therefore, are too weak to be detected above the strong burst continuum. If, on the other hand, the burst emission is isotropic, we show that the disk region where the Fe XXV and FeXXVI lines would be produced is now fully ionized; the neutral iron line could still be at very low levels and masked by the continuum. In that case, however, we would expect a strong BB component, which is not detected. We conclude that, as suggested by Daumerie et al. (1996) and Nishiuchi et al. (1999), the burst emission is highly beamed.

This work was supported under NASA Contract No. NNG08FD60C and made use of data from the *NuSTAR* mission, a project led by the California Institute of Technology, managed by the Jet Propulsion Laboratory, and funded by the National Aeronautics and Space Administration. We thank the *NuSTAR* Operations, Software, and Calibration teams for support with the execution and analysis of these observations. This research has made use of the *NuSTAR* Data Analysis Software (NuSTARDAS) jointly developed by the ASI Science Data Center (ASDC, Italy) and the California Institute of Technology (USA).

REFERENCES

Aleksandrovich, N. L., Borozdin, K. N., Aref'ev, V. A., Sunyaev, R. A., & Skinner, G. K. 1998, AstL, 24, 7
Aptekar, R. L., Butterworth, P. S., Cline, T. L., et al. 1998a, ApJ, 493, 404
Aptekar, R. L., Butterworth, P. S., Cline, T. L., et al. 1998b, ApJ, 493, 408
Arnaud, K. A. 1996, in ASP Conf. Ser. 101, Astronomical Data Analysis Software and Systems V, ed. G. H. Jacoby, & J. Barnes (San Francisco, CA: ASP), 17
Arons, J. 1993, ApJ, 408, 160
Augusteijn, T., Greiner, J., Kouveliotou, C., et al. 1997, ApJ, 486, 1013
Baan, W. A. 1979, ApJ, 227, 987
Ballantyne, D. R., Purvis, J. D., Strausbaugh, R. G., & Hickox, R. C. 2012, ApJL, 747, L35
Barrière, N. M., Tomsick, J. A., Baganoff, F. K., et al. 2014, ApJ, 786, 46
Basko, M. M. 1978, ApJ, 223, 268
Basko, M. M., & Sunyaev, R. A. 1975, A&A, 42, 311
Bautista, M. A., & Kallman, T. R. 2001, ApJS, 134, 139
Becker, P. A., & Wolff, M. T. 2007, ApJ, 654, 435
Bianchi, S., & Matt, G. 2002, A&A, 387, 76
Bianchi, S., Matt, G., Nicastro, F., Porquet, D., & Dubau, J. 2005, MNRAS, 357, 599
Bildsten, L., & Brown, E. F. 1997, ApJ, 477, 897
Bildsten, L., Chakrabarty, D., Chiu, J., et al. 1997, ApJS, 113, 367
Borkus, V. V., Kaniovsky, A. S., Sunyaev, R. A., et al. 1997, AstL, 23, 421
Brazier, K. T. S. 1994, MNRAS, 268, 709
Cannizzo, J. K. 1996, ApJL, 466, L31
Chakrabarty, D., Jonker, P. G., & Markwardt, C. B. 2014, ATel, 5895, 1
Coburn, W., Heindl, W. A., Rothschild, R. E., et al. 2002, ApJ, 580, 394
Cole, D. M., Vanden Berk, D. E., Severson, S. A., et al. 1997, ApJ, 480, 377
Cui, W. 1997, ApJL, 482, L163
D'Ai, A., Di Salvo, T., Iaria, R., et al. 2014, ATel, 5858, 1
Daigne, F., Goldoni, P., Ferrando, P., et al. 2002, A&A, 386, 531
Damen, E., Magnier, E., Lewin, W. H. G., et al. 1990, A&A, 237, 103
D'Angelo, C. R., & Spruit, H. C. 2010, MNRAS, 406, 1208
Daumerie, P., Kalogera, V., Lamb, F. K., & Psaltis, D. 1996, Natur, 382, 141
DeCesar, M. E., Boyd, P. T., Pottschmidt, K., et al. 2013, ApJ, 762, 61
Degenaar, N., Miller, J. M., Harrison, F. A., et al. 2014, ApJL, 796, L9
Fabian, A. C., Rees, M. J., Stella, L., & White, N. E. 1989, MNRAS, 238, 729
Finger, M. H., Jenke, P. A., & Wilson-Hodge, C. 2014, ATel, 5810, 1
Finger, M. H., Koh, D. T., Nelson, R. W., et al. 1996a, Natur, 381, 291

Finger, M. H., Wilson, R. B., & Harmon, B. A. 1996b, ApJ, 459, 288
Fürst, F., Grefenstette, B. W., Staubert, R., et al. 2013, ApJ, 779, 69
Fürst, F., Pottschmidt, K., Wilms, J., et al. 2014a, ApJ, 780, 133
Fürst, F., Pottschmidt, K., Wilms, J., et al. 2014b, ApJL, 784, L40
Ghosh, P., & Lamb, F. K. 1979, ApJ, 232, 259
Giles, A. B., Swank, J. H., Jahoda, K., et al. 1996, ApJL, 469, L25
Gosling, A. J., Bandyopadhyay, R. M., Miller-Jones, J. C. A., & Farrell, S. A. 2007, MNRAS, 380, 1511
Grevesse, N., Noels, A., & Sauval, A. J. 1996, in ASP Conf. Ser. 99, Cosmic Abundances, ed. S. S. Holt, & G. Sonneborn (San Francisco, CA: ASP), 117
Harrison, F. A., Craig, W. W., Christensen, F. E., et al. 2013, ApJ, 770, 103
Hickox, R. C., Narayan, R., & Kallman, T. R. 2004, ApJ, 614, 881
Içdem, B., Inam, S., & Baykal, A. 2011, MNRAS, 415, 1523
Ji, L., Schulz, N., Nowak, M., Marshall, H. L., & Kallman, T. 2009, ApJ, 700, 977
Jimenez-Garate, M. A., Raymond, J. C., Liedahl, D. A., & Hailey, C. J. 2005, ApJ, 625, 931
Kallman, T., & Bautista, M. 2001, ApJS, 133, 221
Kallman, T. R., Angelini, L., Boroson, B., & Cottam, J. 2003, ApJ, 583, 861
Kennea, J. A., Kouveliotou, C., & Younes, G. 2014, ATel, 5845, 1
Koshut, T. M., Kouveliotou, C., van Paradijs, J., et al. 1998, ApJL, 496, L101
Kouveliotou, C., van Paradijs, J., Fishman, G. J., et al. 1996, Natur, 379, 799
Kubota, A., Tanaka, Y., Makishima, K., et al. 1998, PASJ, 50, 667
Lamb, F. K., Fabian, A. C., Pringle, J. E., & Lamb, D. Q. 1977, ApJ, 217, 197
Lasota, J. P., & Pelat, D. 1991, A&A, 249, 574
Lewin, W. H. G., Rutledge, R. E., Kommers, J. M., van Paradijs, J., & Kouveliotou, C. 1996, ApJL, 462, L39
Lewin, W. H. G., van Paradijs, J., & Taam, R. E. 1993, SSRv, 62, 223
Li, L.-X., Zimmerman, E. R., Narayan, R., & McClintock, J. E. 2005, ApJS, 157, 335
Lin, L., Göğüş, E., Kaneko, Y., & Kouveliotou, C. 2013, ApJ, 778, 105
Linares, M., Kennea, J., Krimm, H., & Kouveliotou, C. 2014, ATel, 5883, 1
Masetti, N., D'Avanzo, P., Blagorodnova, N., & Palazzi, E. 2014, ATel, 5999, 1
Matt, G., Brandt, W. N., & Fabian, A. C. 1996, MNRAS, 280, 823
Mejía, J., Villela, T., Goldoni, P., et al. 2002, ApJ, 566, 387
Mihara, T. 1995, PhD thesis, Dept. of Physics, Univ. of Tokyo
Miller, G. S. 1996, ApJL, 468, L29
Miller, J. M., Fabian, A. C., Wijnands, R., et al. 2002, ApJ, 578, 348
Müller, S., Ferrigno, C., Kühnel, M., et al. 2013, A&A, 551, A6
Müller, S., Kühnel, M., Caballero, I., et al. 2012, A&A, 546, A125
Negoro, H., Mihara, T., Kawai, N., et al. 2014a, ATel, 5963, 1
Negoro, H., Sugizaki, M., Krimm, H. A., et al. 2014b, ATel, 5790, 1
Nishiuchi, M., Koyama, K., Maeda, Y., et al. 1999, ApJ, 517, 436
Norris, J. P., Gehrels, N., & Scargle, J. D. 2011, ApJ, 735, 23
Nowak, M. A., Neilsen, J., Markoff, S. B., et al. 2012, ApJ, 759, 95
Ostriker, E. C., & Shu, F. H. 1995, ApJ, 447, 813
Pandey-Pommier, M., Masetti, N., & Durouchoux, P. 2014, ATel, 5904, 1
Paul, B., Dotani, T., Nagase, F., Mukherjee, U., & Naik, S. 2005, ApJ, 627, 915
Pintore, F., Sanna, A., Riggio, A., et al. 2014, ATel, 5901, 1
Porquet, D., & Dubau, J. 2000, A&AS, 143, 495
Porquet, D., Dubau, J., & Grosso, N. 2010, SSRv, 157, 103
Rappaport, S., & Joss, P. C. 1997, ApJ, 486, 435
Reynolds, M. T., & Miller, J. M. 2010, ApJ, 723, 1799
Sanna, A., Pintore, F., Riggio, A., et al. 2014, ATel, 5910, 1
Scargle, J. D., Norris, J. P., Jackson, B., & Chiang, J. 2013, ApJ, 764, 167
Shimura, T., & Takahara, F. 1995, ApJ, 445, 780
Spruit, H. C., & Taam, R. E. 1993, ApJ, 402, 593
Stark, M. J., Baykal, A., Strohmayer, T., & Swank, J. H. 1996, ApJL, 470, L109
Strickman, M. S., Dermer, C. D., Grove, J. E., et al. 1996, ApJL, 464, L131
Suchy, S., Pottschmidt, K., Rothschild, R. E., et al. 2011, ApJ, 733, 15
Taam, R. E., & Lin, D. N. C. 1984, ApJ, 287, 761
Tanaka, Y. 1986, IAU Colloq. 89, Radiation Hydrodynamics in Stars and Compact Objects, Vol. 255, ed. D. Mihalas, & K.-H. A. Winkler (Berlin: Springer), 198
Verner, D. A., Ferland, G. J., Korista, K. T., & Yakovlev, D. G. 1996, ApJ, 465, 487
Wang, Y.-M. 1996, ApJL, 465, L111
Wijnands, R., & Wang, Q. D. 2002, ApJL, 568, L93
Wilms, J., Allen, A., & McCray, R. 2000, ApJ, 542, 914
Woods, P. M., Kouveliotou, C., van Paradijs, J., et al. 1999, ApJ, 517, 431
Woods, P. M., Kouveliotou, C., van Paradijs, J., et al. 2000, ApJ, 540, 1062